8-19-2016

Effect of gap flow on the shallow wake of a sharp-edged bluff body – turbulence parameters

A.M Shinneeb
University of Windsor

R. Balachandar
University of Windsor

CE: SR   **QA:** SR

Taylor & Francis
Taylor & Francis Group

Effect of gap flow on the shallow wake of a sharp-edged bluff body – turbulence parameters

A.-M. Shinneeb and R. Balachandar

Department of Mechanical, Automotive, and Materials Engineering, University of Windsor, Ontario, Canada

ABSTRACT

This experimental study was carried out to investigate the turbulent wake generated by a vertical sharp-edged flat plate suspended in a shallow channel flow with a gap near the bed. The objective of this study is to understand the effect of the gap flow on the turbulent wake by studying two different gap heights between the channel bed and the bottom edge of the bluff body. These two cases were compared to the no-gap case which is considered as a reference case. The maximum flow velocity was 0.45 m/s and the Reynolds number based on the water depth was 45,000. Extensive measurements of the flow field in the vertical mid-plane and in the horizontal near-bed, mid-depth, and near-surface planes were made using particle-image velocimetry (PIV). This paper is the second part of an extensive study to characterise the gap-flow effects and is primarily focused on the mean and instantaneous turbulence quantities as well as coherent structures.

The results revealed that the gap flow increased the transfer of the turbulent kinetic energy (TKE) from the streamwise to the vertical component along the vertical mid-plane. In addition, there is a corresponding increase and spread of the transverse component in the transverse direction as the flow evolves in the downstream direction. The momentum exchange by the Reynolds stress is significantly weak in the vertical mid-plane particularly in the lower half of the water depth, but the gap flow enhanced the momentum exchange in the upper half of the water depth by up to 1% of the freestream velocity squared. Furthermore, the intensity and bursting direction of the turbulence fluctuations in the far field are also affected by the gap flow when it is large. Furthermore, the proper orthogonal decomposition results revealed that the flow contains a large number of structures, and their interactions are responsible for deforming and/or tearing apart the structures, and transferring fluid throughout the velocity field.

1. Introduction

Turbulent wakes generated from two-dimensional bluff bodies have been extensively investigated in the past due to their various applications in engineering. The flow is characterised

---

CONTACT A.-M. Shinneeb ✉ shinneeb@uwindsor.ca

This is a companion paper to *Effect of gap flow on the shallow wake of a sharp-edged bluff body – Mean Velocity Fields* and certain introductory material is duplicated for convenience and completeness.

by the formation of large recirculation zones and periodic (or quasi-periodic) shedding of
vortices. Among these wakes that are commonly encountered in nature is the shallow wake   5
flow. Such flows are generally bounded by a bottom solid wall and a top free surface, gener-
ating a wake region that has characteristics different from the well-known two-dimensional
wakes. In addition, the horizontal width of such shallow wakes is usually larger than the
depth of flow.[1,2]

The behaviour of shallow wakes has been investigated by a number of researchers (e.g.   10
Chen and Jirka,[3] Lloyd and Stansby,[4] Balachandar et al.,[5] Nasif et al. [6]). Akilli and
Rockwell [7] investigated the near wake of a circular cylinder in a shallow flow by means of
flow visualisation and particle-image velocimetry (PIV). They reported mean velocity, vor-
ticity, Reynolds stress, and streamline topology results at three vertical elevations: near the
bed, mid distance, and near the free surface. It was concluded that the vortex formation in   15
the near-wake region is a highly three-dimensional process. Chen and Jirka [3] noted that
the mechanism of vortex stretching does not affect eddies of sizes comparable to the depth
of the flow. It was argued that the resulting wake will carry dual characteristics – the struc-
tures of scales greater than the water depth exhibit inverse cascade in the spectral analysis,
which is an indication of the two-dimensional turbulence. On the other hand, the struc-   20
tures of scale smaller than the flow depth demonstrate the behaviour of three-dimensional
turbulence. More recently, Arindam et al. [8] carried out PIV measurements in the wake of
a sharp-edged bluff body immersed in a shallow channel flow on three horizontal planes
(near the bed, mid depth, and near the free surface) at a Reynolds number, based on the
water depth, of 18,000. The results showed large differences in the size of the recirculation   25
zones between the three horizontal planes. Analysis of the mean flow and vortical structure
results revealed that the entrainment from the sides toward the wake vertical mid-plane
occurs in the three horizontal planes, but with different rates, which was attributed to the
formation and distribution of the vortices near the bed and the free surface.

Numerous experimental and computational studies have been carried out to understand   30
the influence of wall proximity on the flow past long cylinders of different cross-sections
(e.g. circular, square, triangular, etc.). When a bluff body is placed near a plane wall, vor-
tex shedding characteristics and thus transport phenomena in the wake are significantly
affected by the presence of the nearby wall,[9] and in fact vortex shedding can be sup-
pressed completely if the wall is close enough. Because of the influence of vortex shedding   35
on characteristics such as drag and mixing, it is important to understand the influence of
the gap height (h_g) between the wall and the body on the wake flow.[10,11] Examples of
engineering applications of this type of flow are encountered frequently such as the airflow
around solar panels and road vehicles, the cooling of electronic components, and the flow
past pipelines near the ground or in a sea or river bed.   40

Many studies have been carried out with circular cylinders oriented horizontally such
that the cylinder spans the test section and is placed above the bed to form a gap. Bear-
man and Zdravkovich [10] investigated the influence of gap height on the vortex shedding
and the spectral behaviour of the wake as well as the pressure distribution on the wall and
on the cylinder. The experiments were conducted at a Reynolds number of 5×10^4 while   45
the boundary layer thickness was 80% of the cylinder diameter. A critical gap height was
determined such that the vortex shedding was suppressed below this critical value and
becomes independent of the gap height above this value. The influence of the boundary

layer thickness on the behaviour of the turbulent flow past a circular cylinder near a solid
50 plane wall was investigated by Buresti and Lanciotti.[12] It was reported that the effect of
the gap height is strong on the mean velocity and turbulence quantities. Grass et al. [13] and
Taniguchi and Miyakoshi [14] reported that there is a correlation between the critical gap
height and the boundary layer thickness. However, the values reported in the two studies
are different. More recently, Wang and Tan [15] studied the effect of the gap height on the
55 near-wake flow characteristics of a circular cylinder close to the wall using a PIV system
by considering various gap heights. The results included the mean velocity and Reynolds
stress quantities as well as vortical structures. This study confirmed the results of earlier
studies about the effect of the gap height on the vortex shedding.

The effect of the gap height on the wake flow behind square cylinders near a plane wall
60 has also been investigated by a number of researchers (e.g. Taniguchi et al.,[16] Durao et
al.,[17] Bosch et al.,[9] Bailey et al.,[18] Martinuzzi et al. [19]). Similar conclusions as that
noticed in the flow past circular cylinders were reported in these studies, although the val-
ues of the critical gap height and other related parameters were different. On the other hand,
the effect of gap flow on the wake of a flat plate is scarce in literature. Krampa-Morlu and
65 Balachandar [20,21] carried out LDV measurements in the wake of a flat plate suspended   Q1
in a shallow channel flow with a gap height of 5 mm between the plate and the channel
bed. The velocity profiles were measured at downstream locations along the water depth
in the near and intermediate wake regions, and also at upstream locations. In addition, the
velocity profiles were also measured in the transverse direction at two vertical elevations;
70 one in the middle of the water depth, and the other one in the middle of the gap opening.
It was concluded that the flow through the gap resembles the characteristics of a wall jet.
Moreover, the mean velocity and Reynolds shear stress profiles indicated fast recovery of the
flow towards the upstream state in the near-wall region. However, the turbulence intensity
and quadrant analysis results revealed that the flow was still influenced by the disturbance
75 generated by the bluff body, especially away from the wall region.

The present study is an experimental investigation of the interaction of a shallow wake
with a gap flow generated by simple bluff-body geometry. The importance of this research
stems from our desire to gain a better understanding of the turbulence phenomena to
improve methods of prediction and allow better control/exploitation of the dynamic flow
80 features in a variety of engineering applications. Consequently, the use of a global quan-
titative/visualisation tool such as the PIV for investigating the turbulent wake flow is an
attractive option in this effort. The present work then describes a turbulent wake generated
by flows past a vertical sharp-edged flat plate suspended in a shallow channel flow to cre-
ate a gap near the bed. This configuration generates a wall-jet-like flow which would affect
85 the formation of the horseshoe vortex elements near the bed. Extensive PIV measurements
were obtained in the developing wake region at a Reynolds number of 45,000 to quantify
the interaction between the gap flow and the wake. The objective of this study is to under-
stand the effect of the gap flow on the wake by studying two different gap heights between
the channel bed and the bottom edge of the bluff body. These two cases will be compared to
90 the no-gap-flow case which is considered as a reference case. Specifically, this paper is the
second part of an extensive study to characterise the gap-flow effects by investigating the
turbulence quantities and coherent structures to unveil the basic structure of the shallow
wake with gap flow.

2. Experimental apparatus

The present experiments were carried out in a re-circulating open water channel of rectan-   95
gular cross-section. The dimensions of the channel are 9.5 m long, 1.2 m wide, and 0.6 m
deep. The side walls and the bottom of the flume were made of Plexiglas to allow measure-
ments of the flow field using the PIV. The mean freestream velocity U_∞ of the channel flow
was 0.45 m/s. The depth of the water H in the channel was controlled using a tailgate and
nominally maintained at 100 mm in the measurement region. The aspect ratio of the chan-   100
nel flow is 12, which ensures negligible secondary currents. The corresponding Reynolds
number Re_H (based on the water depth H) was 45,000. A flow conditioner consisting of
flow straighteners and wire screens were placed at the entrance of the channel to reduce
turbulence. Measurements were performed at 4.9 m downstream of the flow conditioner.
To ensure fully-developed turbulent flow in the measurement area, the near-wall flow was   105
tripped using a 25 mm wide sand strip spanning the entire channel width and was posi-
tioned at 3 m upstream of the measurement station.

The bluff body used in the present study was a sharp-edged flat plate 110 mm in height,
30 mm in width, and 6 mm in thickness, as shown in Figure 1(a) and 1(b). The bluff body
was designed to have a flat shape on the upstream side while it was chamfered at the edges   110
on the downstream side. The body was inserted vertically in the channel flow, as shown
in Figure 1, and supported by a steel bar from the top of the flume (not shown). Three
positions of the bluff body were considered; one where the bluff body is in physical contact
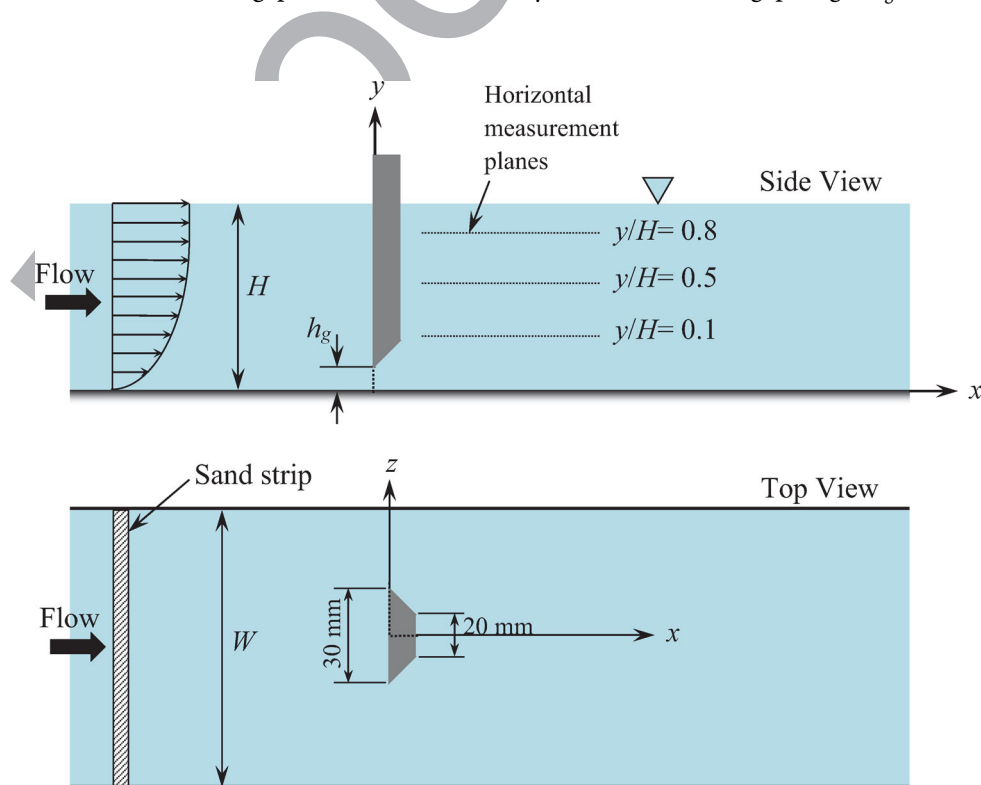with the solid bed (no gap between the bluff body and the solid bed, gap height $h_g = 0$ mm),

Figure 1. Schematic of the bluff body.

115   and two with gap heights h_g of 5 mm and 10 mm, respectively. The first case is known as the no-gap-flow (NGF) case, while the others are known as the small-gap-flow (SGF) and large-gap-flow (LGF) cases. Care was taken to avoid streamwise vibrations of the bluff body. The horizontal confinement in the flume is negligible since the blockage ratio is only 2.5%.

      The origin of the coordinate system adopted in this study is located at the intersection
120   of the vertical line-of-symmetry of the bluff body with the bed of the flume (see Figure 1). The positive x-direction represents the distance measured along the channel flow starting from the origin at the upstream face of the bluff body and will be referred to as the streamwise direction, and the corresponding velocity component u is the mean streamwise velocity. The positive y-direction (measured upward from the bed of the flume) represents
125   the vertical direction with a corresponding mean velocity component v. A right-hand rule was adopted for the coordinate system, and the z-direction was defined accordingly. The z-direction will be referred to as the transverse direction and the corresponding mean velocity is given the symbol w.

3. PIV system and post-processing analysis

130   A TSI PIV system consisting of 120 mJ/pulse dual Nd:YAG lasers (New Wave Research) of 532 nm wavelength was employed in this study. The laser sheet was formed through a 500 mm or 1000 mm spherical lens and a -15 mm or -25 mm cylindrical lens depending on the desired size of the field of view (FOV). The resulting light sheet was approximately 2 mm thick in the area of interest.

135   Measurements will be reported on both vertical $(x; y)$ and horizontal $(x; z)$ planes that span streamwise locations in the range $0 < x/H < 3$. The vertical plane was positioned to cover the entire depth along the vertical mid-plane $(z/H = 0)$. The horizontal planes were positioned at three elevations; near-bed $(y/H = 0.1)$, mid-depth $(y/H = 0.5)$, and near-free-surface $(y/H = 0.8)$ planes. For each case, the velocity field was measured by taking
140   three consecutive FOV downstream of the bluff body. Care was taken in aligning the laser sheet to ensure that the thinnest region of the laser sheet centres the FOV and minimise light reflection near the bed. Table 1 summarises the case name, gap height, location, size, and spatial resolution of each FOV. The water in the flume was seeded with hollow-glass bead seed particles after filtering the water through a 5 μm filter. These particles have a
145   specific gravity of 1.1 and a mean diameter of 10 μm, yielding a Stokes settling velocity of 0.0054 mm/s. Therefore, these particles have the ability to faithfully follow the water flow (see Shinneeb [22] for more details).

      The velocity fields were measured using a 2048×2048 pixels TSI PowerView Plus 4 MP camera and provide 12 bit output. In total, 2000 image pairs were acquired at each location
150   at a framing rate of 1.04 Hz. A TSI PIV LaserPulse synchroniser was used to synchronise the operation of the camera with the laser. The camera was fitted with a 60 mm Micro-Nikkor or a 28–105 mm Zoom-Nikkor lens according to the object's distance, which was adjusted to give the required FOV. Image calibration was achieved by taking a picture of a steel ruler with 1 mm divisions. It was confirmed that there was negligible distortion over the FOV.
155   Image analysis was performed with correlation analysis INSIGHT 3G® software developed by TSI. The images were analysed with 32×32 interrogation areas using a fast-Fourier transform (FFT) correlator. The interrogation areas were overlapped by 50%. The correlation peak was located within subpixel accuracy using a Gaussian curve-fitting

Q2

Table 1. Summary of the velocity field characteristics.

h_g/H	Case name	Vertical position, y/H	Distance from bluff body mm	x/H	Image size (mm × mm)	Spatial resolution (mm)
			Vertical (x, y) planes			
0.00	VSW001	–	− 1.99	− 0.020	70.5 × 70.5	0.55
	VSW002	–	68.09	0.681	103.9 × 103.9	0.81
	VSW003	–	167.34	0.167	103.6 × 103.6	0.81
0.05	VSW051	–	− 1.99	− 0.020	70.5 × 70.5	0.55
	VSW052	–	69.67	0.697	103.9 × 103.9	0.81
	VSW053	–	167.34	0.167	103.6 × 103.6	0.81
0.10	VSW101	–	− 1.99	− 0.020	70.5 × 70.5	0.55
	VSW102	–	68.09	0.681	103.6 × 103.6	0.81
	VSW103	–	167.34	0.167	103.6 × 103.6	0.81
			Horizontal (x, z) planes			
0.00	HSW001A	0.1	0.64	0.006	91.1 × 91.1	0.71
	HSW002A	0.1	74.64	0.746	146.3 × 146.3	1.14
	HSW003A	0.1	175.53	0.176	145.3 × 145.3	1.14
0.05	HSW051A	0.1	0.64	0.006	91.1 × 91.1	0.71
	HSW052A	0.1	74.64	0.075	146.3 × 146.3	1.14
	HSW053A	0.1	175.53	0.176	145.3 × 145.3	1.14
0.10	HSW101A	0.1	0.64	0.006	91.1 × 91.1	0.71
	HSW102A	0.1	74.64	0.075	146.3 × 146.3	1.14
	HSW103A	0.1	175.53	0.176	145.3 × 145.3	1.14
0.00	HSW001B	0.5	− 1.88	− 0.019	101.4 × 101.4	0.79
	HSW002B	0.5	67.10	0.671	157.0 × 157.0	1.23
	HSW003B	0.5	171.45	0.171	153.4 × 153.4	1.20
0.05	HSW051B	0.5	− 1.88	− 0.019	101.4 × 101.4	0.79
	HSW052B	0.5	67.10	0.671	157.0 × 157.0	1.23
	HSW053B	0.5	171.45	0.171	153.4 × 153.4	1.20
0.10	HSW101B	0.5	− 1.88	− 0.019	101.4 × 101.4	0.79
	HSW102B	0.5	67.10	0.671	157.0 × 157.0	1.23
	HSW103B	0.5	171.45	0.171	153.4 × 153.4	1.20
0.00	HSW001C	0.8	− 6.18	− 0.062	103.8 × 103.8	0.81
	HSW002C	0.8	64.69	0.647	164.7 × 164.7	1.29
	HSW003C	0.8	165.44	0.165	164.0 × 164.0	1.28
0.05	HSW051C	0.8	− 6.18	− 0.062	103.8 × 103.8	0.81
	HSW052C	0.8	64.69	0.647	164.7 × 164.7	1.29
	HSW053C	0.8	165.44	0.165	164.0 × 164.0	1.28
0.10	HSW101C	0.8	− 6.18	− 0.062	103.8 × 103.8	0.81
	HSW102C	0.8	64.69	0.647	164.7 × 164.7	1.29
	HSW103C	0.8	165.44	0.165	164.0 × 164.0	1.28

method. This analysis process yielded a final spatial resolution of 16 pixels. Table 1 summarises the size and the resulting spatial resolution of the velocity fields reported in this paper. Note that the *Distance from Bluff Body* column represents the streamwise distance from the bluff body to the left edge of the FOV. Following the correlation analysis, outliers were rejected using the cellular neural network method with a variable threshold technique, as proposed by Shinneeb et al. [23]. The percentage of vectors rejected varied from 3% to 6% primarily at the edges of the velocity fields. Rejected vectors were replaced using a Gaussian-weighted mean of their neighbours.

4. Uncertainty analysis

The uncertainty of the PIV data is generally a function of the experimental settings (the flow conditions and image acquisition) and the image correlation analysis.[24] The error sources

170 of the experimental conditions usually come from the instruments calibration, image cali-
bration, image distortion, etc. whereas the image correlation analysis is influenced by par-
ticle image size, interrogation area size, particle seeding density, computational techniques,
velocity gradients, and three-dimensional (out of plane) motion. In this study, the experi-
ments were carried out carefully to reduce the uncertainty and the maximum error in the
175 velocity U_∞ at inlet is estimated to be 1.57%. Moreover, the error sources during the image
acquisition can arise from the position and alignment of the calibration ruler compared to
the laser sheet, as well as the accuracy of identifying pixel distance on the ruler-graduation
image. The errors are estimated to be 0.5 mm, 2º, and 1 pixel, respectively (see the guide-
line of uncertainty analysis of PIV dataset proposed by the International Towing Tank Con-
180 ference 2008 for more details). Thus, the total uncertainty of the experimental conditions
becomes 0.02%.

To quantify the uncertainty that comes from the image correlation algorithms, the
analysis was performed by generating synthetic images with characteristics similar to the
real images and known values of the particle displacements. As described in Bugg and
185 Rezkallah[26], the characteristics of the simulated images were quantified by the following
parameters: background noise, number of paired and spurious particles, particle diameter,
particle intensity and displacement magnitude. These characteristics were obtained from
the real images using Matlab software. The simulated images were then analysed using the
same procedures applied to the real images, and the outliers were detected and replaced
190 using the same techniques as in the real data. Finally, both systematic and random uncer-
tainties were determined by comparing the known and measured particle displacements.
Thus, the relative uncertainty of the maximum displacement (8 pixels) of the instantaneous
velocity fields is found to be about 1.43%. Including the error in the experimental settings,
the relative error for the instantaneous velocity fields becomes 2.12%. Consequently, the
195 relative error of the fluctuating velocity field, which increases by about one order of mag-
nitude (see also Shinneeb [22] for similar analysis).

5. Results and discussions

This section presents the instantaneous and mean turbulence quantity fields in the wake
of a shallow bluff body at different gap heights $h_g/H = 0$, 0.05, and 0.10. The gap height
200 $h_g/H = 0$ is called the NGF case and is used as a reference case, while the other two cases
are referred to as SGF and LGF cases. The Reynolds number, based on the water depth H,
is 45,000.

5.1. Mean turbulence quantities

A global representation of the distribution of the streamwise u_{rms} and vertical v_{rms} turbu-
205 lence intensities along the vertical mid-plane ($z/H = 0$) is given in Figure 2. This figure
consists of six colour contour plots of u_{rms} and v_{rms} superimposed on the mean velocity
field, where each row presents the colour contours of u_{rms} and v_{rms} at a specific gap height
($h_g/H = 0$, 0.05, or 0.10). In these plots, locations x and y are normalised by the water
depth H and the velocities are normalised by the free stream velocity U_∞. Figure 2(a) and
210 2(b) displays colour contours of u_{rms}/U_∞ and v_{rms}/U_∞ in the NGF case ($h_g/H = 0$). These
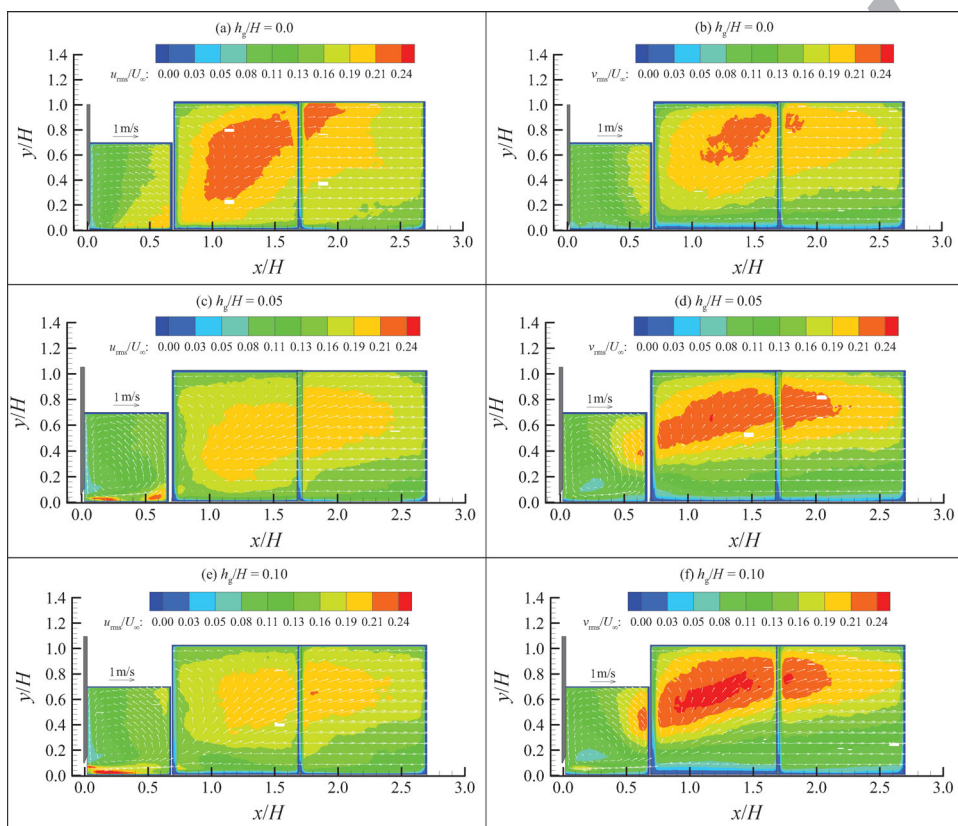plots show the distribution of u_{rms}/U_∞ and v_{rms}/U_∞, which illustrate larger magnitude of

Figure 2. Contours of the streamwise u_{rms} (a, c, and e) and vertical v_{rms} (b, d, and f) turbulence intensities superimposed on the mean velocity fields. These results are extracted from the vertical mid-plane ($z/H = 0.0$). Each row presents the results at a specific gap height ($h_g/H = 0$, 0.05, and 0.10). Locations (x and y) are normalised by H and velocities (u_{rms} and w_{rms}) by U_∞.

$u_{\mathrm{rms}}/U_\infty$ over a wide area than $v_{\mathrm{rms}}/U_\infty$. It is interesting to see that these plots illustrate a gradual increase of $u_{\mathrm{rms}}/U_\infty$ and $v_{\mathrm{rms}}/U_\infty$ starting from the bed and spreads to the free surface as the flow develops in the downstream direction. This behaviour suggests a transfer of the turbulent kinetic energy (TKE) from the transverse component w_{rms} (near the bed) to the streamwise u_{rms} and/or vertical v_{rms} components. As the gap flow increases to $h_g/H = 0.05$, Figure 2(c) and 2(d) displays a reduction in the magnitude of $u_{\mathrm{rms}}/U_\infty$ (excluding the small regions near the bed in the first FOV) with a corresponding increase of $v_{\mathrm{rms}}/U_\infty$. The reduction in the magnitude of $u_{\mathrm{rms}}/U_\infty$ and the corresponding increase of $v_{\mathrm{rms}}/U_\infty$ increases with increasing the gap flow to $h_g/H = 0.10$, as shown in Figure 2(e) and 2(f). These results illustrate clearly an increase in the transfer of the TKE from the streamwise component u_{rms} to the vertical component v_{rms} as the gap flow increases.

To shed light on the behaviour of the turbulence intensity in the near-bed horizontal plane ($y/H = 0.1$), three pairs of $u_{\mathrm{rms}}/U_\infty$ and $w_{\mathrm{rms}}/U_\infty$ plots are presented as colour contours in Figure 3. The velocity field in this plane is more affected by the gap flow than the upper planes and, due to the space limitation and similarity between the results, it is the only plane discussed in this section. The $u_{\mathrm{rms}}/U_\infty$ and $w_{\mathrm{rms}}/U_\infty$ colour contour results, as shown
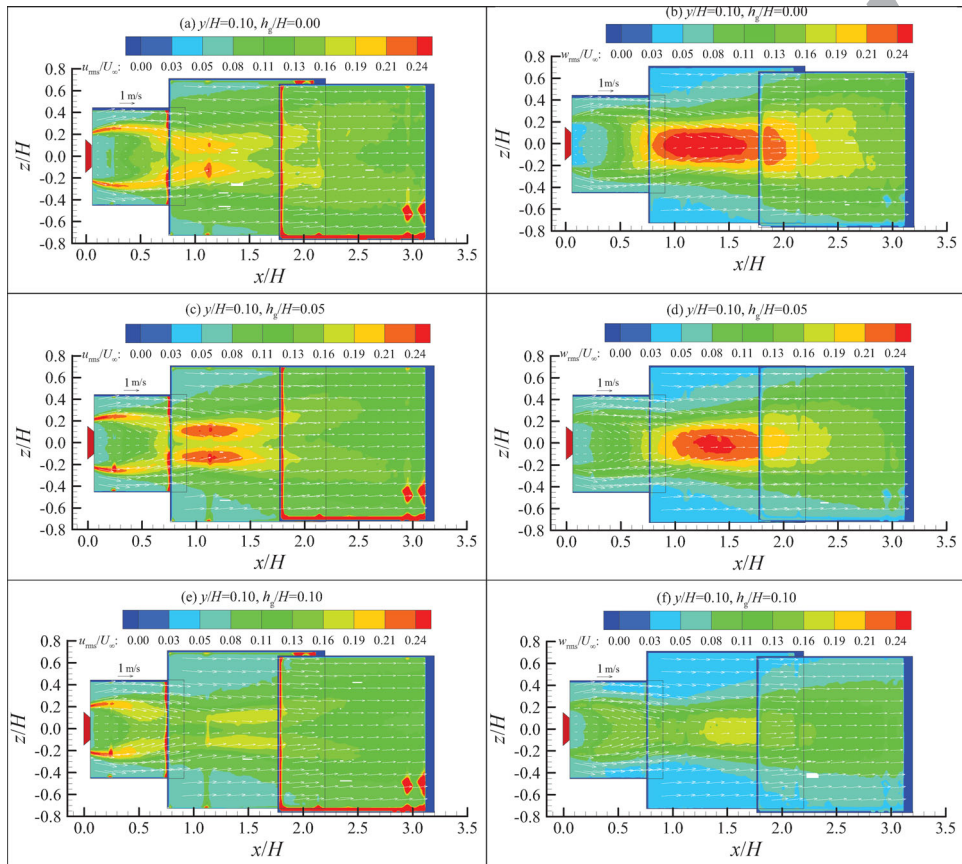
Figure 3. Contours of the streamwise u_{rms} (a, c, and e) and transverse w_{rms} (b, d, and f) turbulence intensities superimposed on the mean velocity fields. These results are extracted from the near-bed horizontal plane ($y/H = 0.1$). Each row presents the results at a specific gap height ($h_g/H = 0, 0.05,$ and 0.10). Locations (x and y) are normalised by H and velocities (u_{rms} and w_{rms}) by U_s.

in Figure 3(a) and 3(b), display that w_{rms} is more energetic than u_{rms} in the core region ($|z/H| < 0.2$), and extends in the downstream direction, while u_{rms} is generally weaker. For the SGF case ($h_g/H = 0.05$), Figure 3(c) and 3(d) shows a slight increase of u_{rms} (in the highest u_{rms} region) near the vertical mid-plane in the region $0.8 < x/H < 1.7$, and a shrink (decrease) in the area of the highest magnitude of w_{rms}. This region is actually characterised by the formation of a pair of recirculation zones as discussed in the mean velocity results (see the first part of this study). As the gap flow increases to $h_g/H = 0.10$, Figure 3(e) and 3(f) shows a significant reduction of the highest values of u_{rms}/U_∞ and w_{rms}/U_∞ in the core region, which supports our observation of the transfer of the TKE from w_{rms} to u_{rms}, and then to v_{rms} as shown in Figure 2. More discussion about the distribution of the turbulence intensity quantities is given below.

5.2. Streamwise variation of the turbulence intensities along the vertical mid-plane

The development of the mean streamwise u_{rms}, vertical v_{rms}, and transverse w_{rms} turbulence intensities in the streamwise direction x along the vertical mid-plane ($z/H = 0$) is shown in
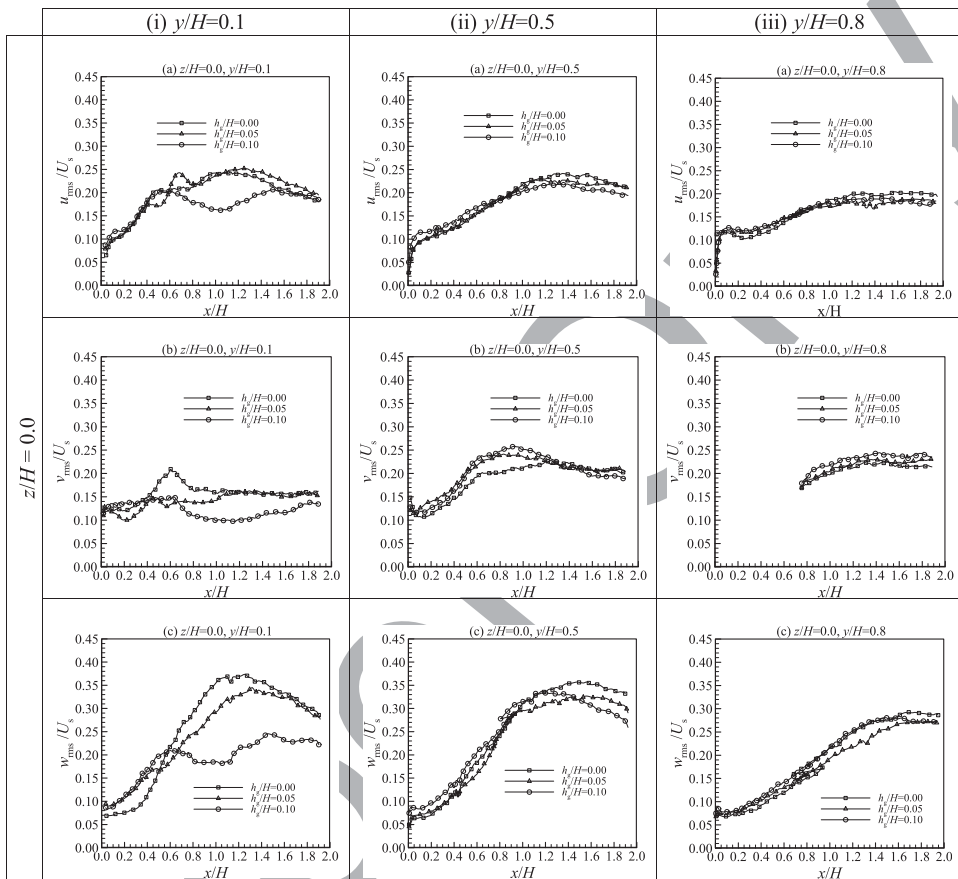
Figure 4. Variation of the streamwise u_{rms}, vertical v_{rms}, and transverse w_{rms} turbulence intensities in the streamwise direction x along the vertical mid-plane ($z/H = 0$) extracted from three vertical locations; (i) $y/H = 0.1$, (ii) $y/H = 0.5$, and (iii) $y/H = 0.8$. Velocities (u_{rms}, v_{rms}, and w_{rms}) are normalised by U_s and streamwise locations x by H.

Figure 4. This figure consists of three columns which represent the three horizontal planes at vertical locations; (i) $y/H = 0.1$, (ii) $y/H = 0.5$, and (iii) $y/H = 0.8$, respectively. Each column consists of three plots (a, b, and c), which display u_{rms}, v_{rms}, and w_{rms} profiles, respectively. Each plot presents the profiles for all three gap heights ($h_g/H = 0$, 0.05, and 0.10). In these plots, u_{rms}, v_{rms}, and w_{rms} are normalised by the mean streamwise velocity U_s of the channel flow without the body ($U_s = 0.330$ m/s, 0.420 m/s, and 0.445 m/s for $y/H = 0.1$, 0.5, and 0.8, respectively), and x is normalised by the water depth H. This velocity scale (U_s) represents the local velocity and is chosen because it can produce comparable dimensionless velocity magnitudes between the three horizontal velocity fields. Note that only some symbols are shown to avoid cluttering.

The relative streamwise turbulence intensity u_{rms}/U_s profiles are shown in the first row of Figure 4. The general trend of the profiles in the three planes is the high rate of increase of u_{rms}/U_s just behind the bluff body, followed by a lower rate of increase to $x/H \approx 1.3$, and then a gradual decrease at further downstream locations. In addition, plot (a) of Figure 4(i)–(iii) shows that the effect of gap flow on u_{rms}/U_s in the vertical mid-plane ($z/H = 0$) seems to be restricted to only the near-bed plane ($y/H = 0.1$), whereas its effect is negligible on the

TJOT_A_1088156 TFJATS_StdSerif-B5.cls September 10, 2015 21:43 Trim Info: 174mm × 248mm

JOURNAL OF TURBULENCE ⊛ 11

upper planes. By comparing with the NGF case, plot (a) of Figure 4(i) illustrates that the effect of the gap flow on the SGF case occurs mainly in the range $x/H \approx 0.4$ to 0.7 (similar to a sine wave cycle), and then follow closely the NGF ($h_g/H = 0$) curve. This sine-wave behaviour is coincident with the symmetrical plane of the two small recirculation zones formed in that region (see Figure 3(b) and the first paper). On the other hand, the effect of the LGF ($h_g/H = 0.10$) on u_{rms}/U_s is apparent at farther streamwise locations, where u_{rms}/U_s gradually decreases to its minimum value of ~0.16 at $x/H \approx 1.04$, and then increases again to the same turbulence level as the other cases for $x/H > 1.5$. In the upper planes ($y/H = 0.5$ and 0.8), plot (a) of Figure 4(ii) and 4(iii) shows that the difference between the profiles in these planes is relatively small (falls within the uncertainty limits of the results). The maximum level of turbulence in the mid-depth and the near-surface planes is approximately $u_{rms}/U_s \approx 0.23$ and 0.18, respectively, which occurs at $x/H \approx 1.34$.

The second row of Figure 4 presents the development of the relative vertical turbulence intensity v_{rms}/U_s in the downstream direction in the three planes. The significant effect of the gap flow can be seen on v_{rms}/U_s only in the near-bed and mid-depth velocity fields. Plot (b) of Figure 4(i) shows that the level of v_{rms}/U_s in the near-bed plane is generally lower than the corresponding u_{rms}/U_s level. In addition, the effect of the gap flow on v_{rms} in the SGF and LGF cases occurs approximately in the same streamwise region as the u_{rms}/U_s profiles, where v_{rms}/U_s in the LGF case loses approximately 40% of its energy compared to the NGF case ($v_{rms}/U_s \approx 0.16$). In the mid-depth plane, plot (b) of Figure 4(ii) shows that the effect of the gap flow becomes relatively large in the range $0.6 < x/H < 1.2$, where v_{rms}/U_s in the SGF and LGF cases becomes approximately 14% and 24% higher than the NGF case. This increase is consistent with the results shown in Figure 2. The vertical turbulence fluctuations v' in the near-surface plane, shown in plot (b) of Figure 4(iii), appear to be approximately equal in the range $x/H > 0.8$. Note that there is no data for $x/H < 0.8$ because the first FOV does not cover the whole water depth H.

The third row of Figure 4 shows that the transverse turbulence intensity w_{rms} component is the most energetic portion of the TKE, and the gap flow affects mainly the near-bed plane and lesser the mid-depth plane. Moreover, the SGF and LGF cases are affected at similar streamwise locations as other turbulence intensity components discussed above. Plot (c) of Figure 4(i) shows that the transverse turbulence fluctuations w' appear to be significantly inhibited by the gap flow at farther downstream locations ($x/H > 0.5$), where the maximum suppression of the SGF and LGF cases is quantified to be ~17% and ~50% smaller than the NGF case. In the mid-depth and near-surface planes, the w_{rms}/U_s profiles of the three gap height cases, shown in plot (c) of Figure 4(ii) and 4(iii), appear to grow with the same rate and a relatively small difference in the magnitude. However, the effect of the gap flow on the mid-depth plane is noticeable only at farther downstream locations ($x/H > 1.0$), whereas in the near-surface plane, the difference between the three cases is really small (falls within the uncertainty limits). Generally, the gap flow appears to mildly inhibit the turbulence fluctuations in the SGF and significantly in the LGF case.

5.3. Turbulence intensity profiles

Vertical plane

Profiles of the relative streamwise turbulence intensity u_{rms}/U_∞ extracted from the vertical mid-plane at different streamwise locations are shown in Figure 5(a)–(f) for the $h_g/H = 0$, 0.05, and 0.10 cases. In these figures, u_{rms}/U_∞ is plotted against the vertical axis y/H.
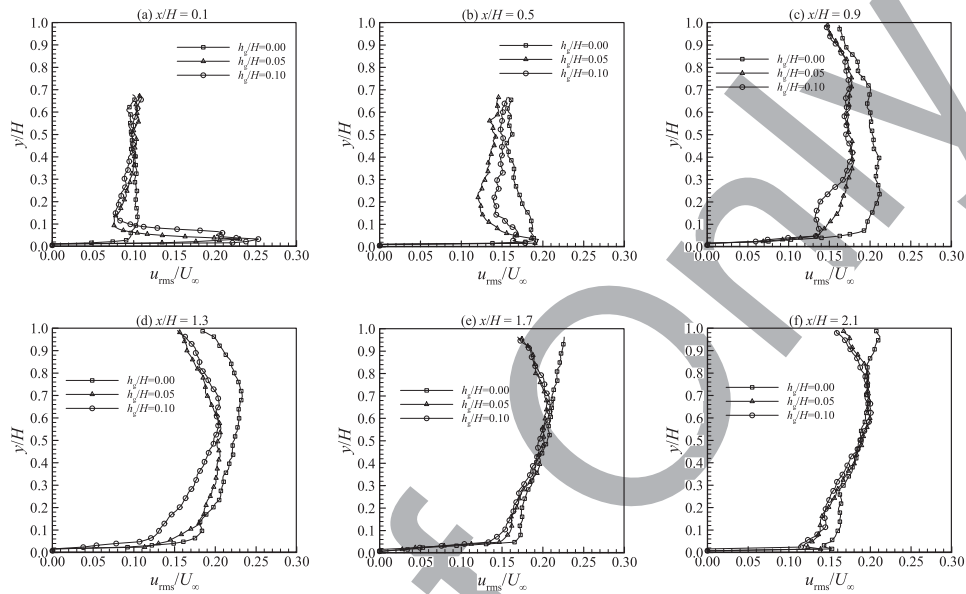
Figure 5. The relative streamwise turbulence intensity u_{rms}/U_∞ profiles measured on the vertical mid-plane ($z/H = 0$) at different streamwise locations; (a) $x/H = 0.1$, (b) $x/H = 0.5$, (c) $x/H = 0.9$, (d) $x/H = 1.3$, (e) $x/H = 1.7$, and (f) $x/H = 2.1$. The velocity u_{rms} is normalised by U_∞ and locations y by the water depth H.

Figure 5(a) shows the u_{rms}/U_∞ profiles for the three gap height cases at a streamwise location $x/H = 0.1$. A comparison between the three profiles shows that u_{rms}/U_∞ for the two gap-flow cases ($h_g/H = 0.05$ and 0.10) is greater near the solid wall ($y/H < 0.1$) with 305 peaks of $u_{rms}/U_\infty \approx 0.23$ and 0.25 located at $y/H \approx 0.03$. The percentage of increase in the SGF and LGF cases is ~130% and ~153%, respectively, as compared with the NGF case which appears almost uniform with $u_{rms}/U_\infty \approx 0.10$. This sharp increase in the energy is obviously boosted by the gap flow. It is interesting to see that this sharp increase in u_{rms}/U_∞ near the bed is accompanied by a corresponding decrease at higher vertical locations ($0.1 <$ 310 $y/H < 0.4$), which is likely entrained by the gap flow/jet. Above that ($y/H > 0.4$), the three profiles become almost equal away from the solid wall. At $x/H = 0.5$, Figure 5(b) shows that the level of the streamwise fluctuations u' in the SGF and LGF cases become smaller than the NGF case. However, the u_{rms}/U_∞ profile of the SGF case still shows a relatively sharp peak ($u_{rms}/U_\infty \approx 0.19$) near the bed located at $y/H \approx 0.03$, and appears the smallest with 315 a constant value of $u_{rms}/U_\infty \approx 0.14$; whereas the level of the streamwise fluctuations in the LGF case appears in the middle between the two cases. The trend of the three cases does not seem to be consistent with the increase of the gap heights due to the redistribution of the TKE as will be discussed in the Figure 6. As the flow develops to $x/H = 0.9$, Figure 5(c) shows that u_{rms}/U_∞ in the SGF and LGF cases is still smaller than the NGF case and matches 320 each other over most of the water depth, although the streamwise fluctuations in the LGF cases appear to be more inhibited near the bed ($0.05 < y/H < 0.4$) by the gap flow. Further downstream, Figure 5(d) shows that the shape of the u_{rms}/U_∞ profiles at $x/H = 1.3$ becomes more circular than the profiles at previous locations where the maximum u_{rms}/U_∞ occurs in the mid-depth region. This figure shows that the magnitude of u_{rms}/U_∞, in the three 325
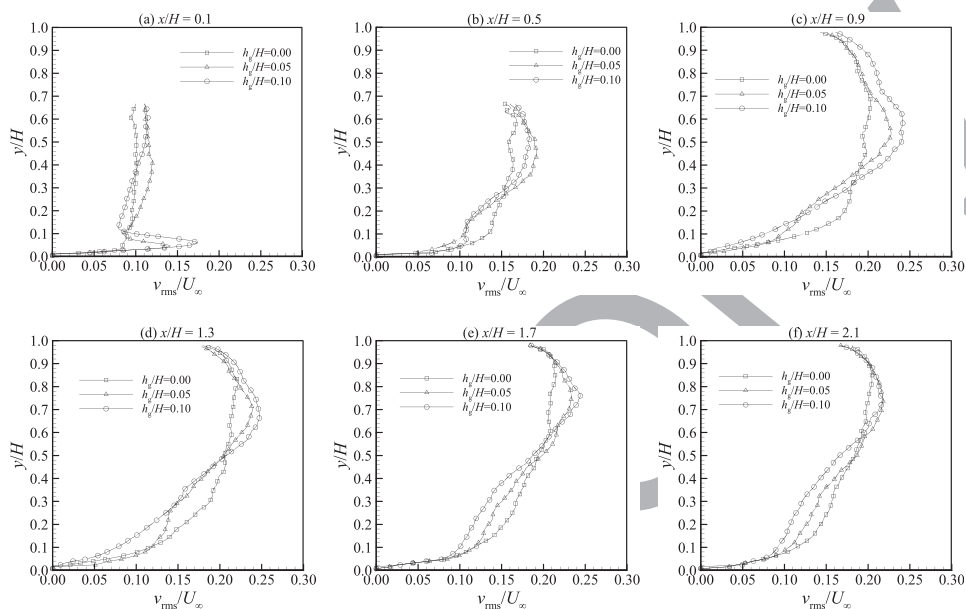
Figure 6. The relative vertical turbulence intensity v_{rms}/U_∞ profiles measured on the vertical mid-plane ($z/H = 0$) at different streamwise locations; (a) $x/H = 0.1$, (b) $x/H = 0.5$, (c) $x/H = 0.9$, (d) $x/H = 1.3$, (e) $x/H = 1.7$, and (f) $x/H = 2.1$. The velocity v_{rms} is normalised by U_∞ and locations y by the water depth H.

cases, becomes even larger at this streamwise location compared to the previous location, and the largest u_{rms}/U_∞ is still attained by the NGF case. By comparing the three cases, it can be observed that the streamwise fluctuations u' of the SGF and LGF case are suppressed throughout the water depth by the gap flow. However, the streamwise fluctuations u' of the

330   SGF profile, in the lower half of the water depth, appear to be close in magnitude to the NGF case, whereas, in the upper half of the water depth, it matches the LGF case. Moreover, it can be observed that u_{rms}/U_∞ decreases near the boundaries in the SGF and LGF profiles (compared to the previous location) with a corresponding increase inside the water layer (far from the boundaries). This behaviour suggests that the streamwise turbulence energy

335   is redistributed throughout the water layer as a result of the gap flow.

At farther downstream location ($x/H = 1.7$), Figure 5(e) illustrates that u_{rms}/U_∞ decreases in the lower half of the water layer in the NGF and SGF cases compared to the previous location; but, in the LGF case, there is a slight increase. In addition, there is a corresponding increase in u_{rms}/U_∞ near the free surface ($y/H > 0.85$) in all cases particularly the

340   NGF case. This indicates that u_{rms} is increasing throughout the water depth in the LGF case, while u_{rms} is redistributed throughout the water layer in the NGF and SGF cases. Further downstream ($x/H = 2.1$), Figure 5(f) shows that u_{rms}/U_∞ continues to decrease throughout the water layer particularly in the lower half of the water depth. Near the free surface ($y/H > 0.85$), the NGF case still maintains the highest u_{rms}/U_∞ as compared with the other cases,

345   although it slightly decreased compared to the previous streamwise location. The reduction of u_{rms}/U_∞ will continue throughout the water depth at farther downstream locations particularly in the upper half of the water layer as confirmed by our results (not shown because of space limitation). All these results indicate that the flow is still developing.

The profiles of the relative vertical turbulence intensity $v_{\mathrm{rms}}/U_\infty$ along the vertical mid-plane are shown in Figure 6(a)–(f). The $v_{\mathrm{rms}}/U_\infty$ profiles at $x/H = 0.1$, shown in Figure 6(a), display similar behaviour and comparable magnitudes to the $u_{\mathrm{rms}}/U_\infty$ profiles shown in Figure 5(a). It is interesting to see that the level of the vertical fluctuations v' in the SGF and LGF cases is generally larger in magnitude than the NGF case, and characterised by spikes near the bed ($y/H < 0.13$) with values 0.14 and 0.17, respectively; located at $y/H \approx$ 0.05; whereas the NGF case appears almost uniform in this figure ($v_{\mathrm{rms}}/U_\infty \approx 0.10$). At a streamwise location $x/H = 0.5$, Figure 6(b) shows a rapid increase of the vertical fluctuations v' in the vertical direction away from the bottom solid boundary, compared to the $u_{\mathrm{rms}}/U_\infty$ results at the same location. Although the increase of $v_{\mathrm{rms}}/U_\infty$ in the NGF case is larger in the lower region ($y/H < 0.28$) than the other cases, this behaviour is reversed above this point to become the smallest at this streamwise location. These results indicate that the energy is transferred from the lower side of the water layer to the upper side triggered by the gap flow. It is interesting to see that the largest $v_{\mathrm{rms}}/U_\infty$ in the upper side ($y/H > 0.28$) is reached by the SGF case at this location, which is consistent with our observation of the complete engulfment of the gap flow by the recirculation zone in the SGF case discussed in the first part of this work. As the flow evolves to $x/H = 0.9$, the upward transfer of energy seems to continue which leads to a significant increase in the magnitude of $v_{\mathrm{rms}}/U_\infty$ in all cases particularly the SGF and LGF cases. However, the largest magnitude of $v_{\mathrm{rms}}/U_\infty$ in the lower region of the water layer ($y/H < 0.31$) is attained by the NGF case. The peak values of the SGF and LGF cases are $v_{\mathrm{rms}}/U_\infty \approx 0.23$ and 0.24, respectively, located at $y/H \approx 0.68$. The large increase of $v_{\mathrm{rms}}/U_\infty$ in the upper side is consistent with the upward flow discussed in the first part of this study (see Figure 4 in the first paper). In addition, the decrease of $u_{\mathrm{rms}}/U_\infty$ of the SGF and LGF cases in Figure 5(d) and the increase of $v_{\mathrm{rms}}/U_\infty$ in Figure 6(d) reveal a redistribution of the TKE that takes place as a result of the gap flow.

The upward transfer of the energy in the vertical direction continues in the downstream direction as shown in Figure 6(d) and 6(e). At $x/H = 1.3$, Figure 6(d) shows that, in the upper half of the water depth, the vertical turbulence fluctuations v' of the SGF and LGF cases still appear larger in magnitude than the NGF case, with peak values of $v_{\mathrm{rms}}/U_\infty \approx$ 0.24 and 0.25, respectively, shifted upward to $y/H \approx 0.67$. In addition, the vertical fluctuations v' of the NGF appear to expand in the lower half of the water depth ($y/H < 0.5$) and become the largest in magnitude. At a streamwise location $x/H = 1.7$, Figure 6(d) shows that $v_{\mathrm{rms}}/U_\infty$ of the three cases seem to have reached the maximum values and started decreasing in the lower half of the water depth. The fluctuations in the NGF case appears the strongest in the lower half of the water depth ($y/H < 0.48$), but it becomes the weakest in the upper half. In addition, the peaks of the SGF and LGF cases, which appear to be shifted upwards towards the free surface ($y/H \approx 0.75$), are $v_{\mathrm{rms}}/U_\infty \approx 0.23$ and 0.24, respectively. At further streamwise location ($x/H = 2.1$), the vertical fluctuations v' appear to decrease slightly throughout the water layer at this streamwise location as shown in Figure 6(f). The vertical fluctuations of the SGF and LGF cases become equal close to the free surface, with a peak magnitude of $v_{\mathrm{rms}}/U_\infty \approx 0.22$.

In summary, the results reveal a decrease of $u_{\mathrm{rms}}/U_\infty$ of the SGF and LGF cases with a corresponding increase of $v_{\mathrm{rms}}/U_\infty$ which suggests a redistribution of the TKE in the gap-flow cases. In addition, the results also show a systematic increase of the vertical fluctuations v' in the vertical direction away from the bottom solid boundary, compared to the streamwise turbulence fluctuations u'. As well, it is observed that $v_{\mathrm{rms}}/U_\infty$ in the SGF is the largest

395 in the upper side ($y/H > 0.28$) in the streamwise distance $x/H \leq 0.5$, which is consistent with the complete engulfment of the gap flow by the recirculation zone discussed in the first part of this work. On the other hand, the streamwise fluctuations u' in the NGF case appear to be the strongest over most of the water depth and close to uniform, whereas the vertical fluctuations v' are the strongest in the lower half of the water layer.

Horizontal plane profiles

400 The development of the streamwise turbulence intensity u_{rms} profiles in the streamwise direction at $x/H = 0.1, 0.5, 0.9, 1.3, 1.7$, and 2.1 extracted from the near-bed ($y/H = 0.1$), mid-depth ($y/H = 0.5$), and near-surface ($y/H = 0.8$) planes, respectively, are presented in three columns (i, ii, and iii) as shown in Figure 7. Each column consists of six plots and

405 each plot presents the profiles for all three gap heights ($h_g/H = 0, 0.05$, and 0.10). In these figures, u_{rms} is normalised by the upstream mean velocity U_s and z by the water depth H. It should be recalled that some small differences between the profiles may be affected by the measurement errors, and does not represent flow physics. Plot (a) in Figure 7(i)–(iii) shows the distribution of the u_{rms}/U_s profiles at a streamwise location $x/H = 0.1$. Generally, all the

410 profiles in these plots appear symmetrical about the vertical mid-plane ($z/H = 0$) with two distinct spikes at the sides and a valley between them. Note that the edges of the bluff body are at $z/H = \pm 0.15$. In the near-bed plane, plot (a) of Figure 7(i) shows that the off-axis peaks for $h_g/H = 0, 0.05$, and 0.10 are approximately equal ($u_{rms}/U_s \approx 0.34 \pm 0.01$) in the near-bed plane, located at $|z/H| \approx 0.23$; whereas u_{rms}/U_s in the valley is uniform and approximately

415 $u_{rms}/U_s \approx 0.10 \pm 0.01$. It can be observed that only the turbulence fluctuations of the LGF case increased by $\sim$20% in the valley as a result of the gap flow. Similarly, the off-axis peaks of u_{rms}/U_s in the mid-depth and near-surface planes, shown in plot (a) of Figure 7(ii) and 7(iii), are relatively smaller than those in the near-bed plane, and equal to $u_{rms}/U_s \approx 0.28 \pm 0.02$; while the turbulence level in the valley is larger in the near-surface plane (u_{rms}/U_s

420 $\approx 0.12 \pm 0.01$), compared to the mid-depth plane ($u_{rms}/U_s \approx 0.10 \pm 0.01$).

As the flow proceeds in the downstream direction, the plots show that the effect of the gap flow is significant on u_{rms}/U_s only in the near-bed plane, while its effect is mild/negligible on the upper planes. Plot (b) of Figure 7(i) shows that, the magnitude of u_{rms}/U_s is almost equal in the outer side ($|z/H| > 0.22$) for the three gap height cases, where

425 the magnitude of the off-axis peaks is $u_{rms}/U_s \approx 0.26 \pm 0.01$. Conversely, the valleys of the three gap cases appear different in magnitude and/or shape. Specifically, the NGF case takes a W-shape with $u_{rms}/U_s \approx 0.21$ at $z/H = 0$; whereas, in the SGF and LGF cases, it takes a U-shape with $u_{rms}/U_s \approx 0.17$ and 0.20, respectively. By inspecting the vector plots (Figure 5 in the first paper) to investigate the difference between the valley shapes, it is found that

430 two small recirculation zones were formed in the NGF case at the sides of the vertical mid-plane ($z/H = 0$) in the streamwise range $0.42 < x/H < 0.72$ (their centres are approximately located at $x/H = 0.5$ and $z/H = \pm 0.06$). These zones triggered a reverse flow in the vertical mid-plane region, which increased the streamwise fluctuations u' near the vertical mid-plane, and then gradually decreased at the sides away from the vertical mid-plane. As the

435 flow evolves downstream, plots (c)–(e) of Figure 7(i) show that the largest off-axis peaks are attained by the SGF case from $x/H = 0.9$ to 1.7; whereas the smallest peaks and valley are reached by the LGF case. Moreover, the largest level of the streamwise fluctuations u' at the outer sides of the profiles ($|z/H| > 0.19$) was attained by the NGF case, and decreases as the gap flow increases. It is interesting to see that the narrowing of the NGF and SGF profiles

at the sides is accompanied with a corresponding increase of the off-axis peaks, which sug-   440
gests a redistribution of u_{rms} in the transverse direction. On the other side, the lowest level
of u_{rms}/U_s in the LGF case ($h_g/H = 0.10$) reflects the large suppression of the streamwise
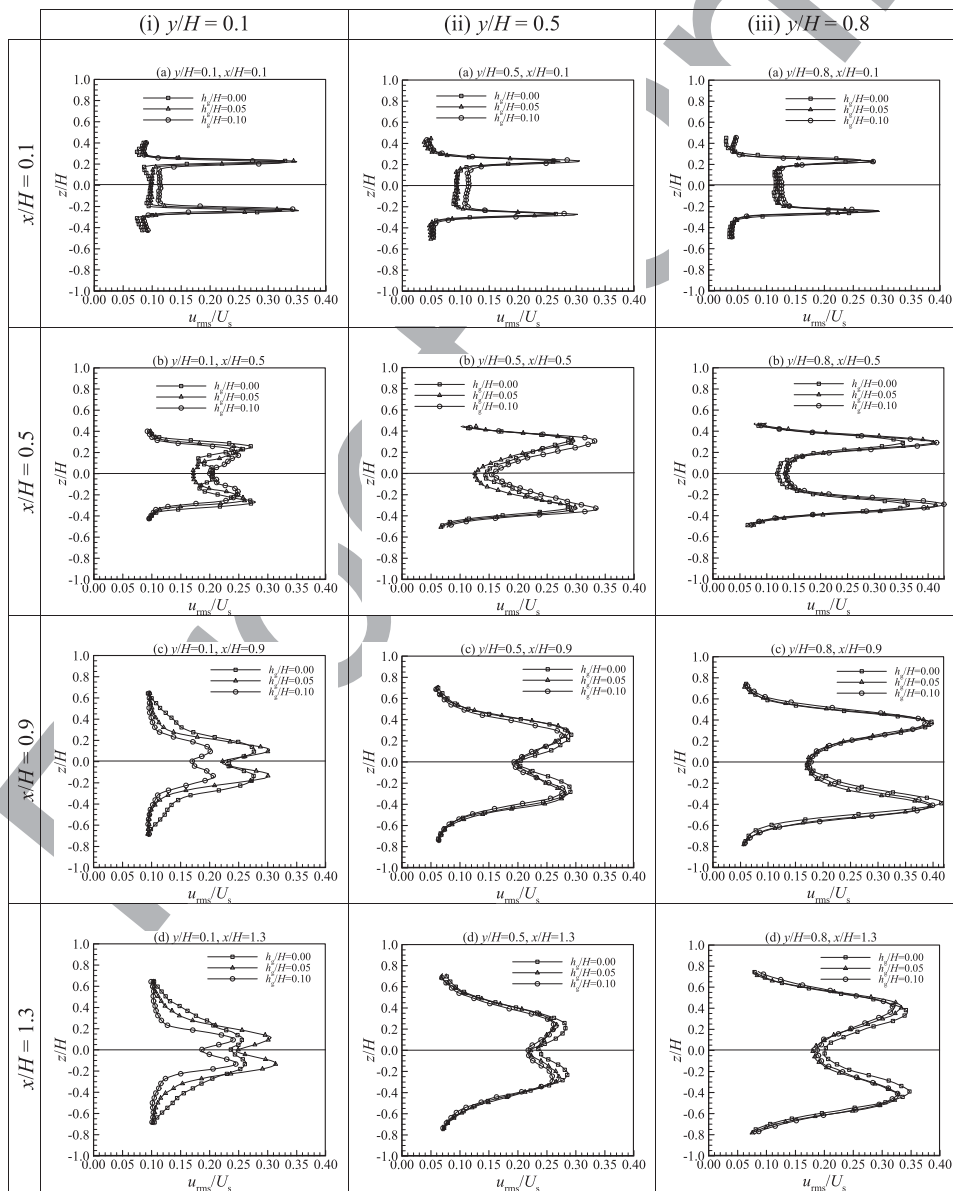fluctuations u' by the gap flow. At $x/H = 2.1$, plot (f) of Figure 7(i) reveals widening of the

Figure 7. The relative streamwise turbulence intensity u_{rms}/U_s profiles measured on the horizontal plane at; (i) $y/H = 0.1$, (ii) $y/H = 0.5$, and (iii) $y/H = 0.8$. Each column (i, ii, and iii) consists of six plots (a, b, c, d, e, and f) which display the development of u_{rms} profiles in the streamwise direction x. Each plot presents u_{rms}/U_s profiles for gap heights $h_g/H = 0.0$, 0.05, and 0.10. u_{rms} is normalised by U_s and z by the water depth H.
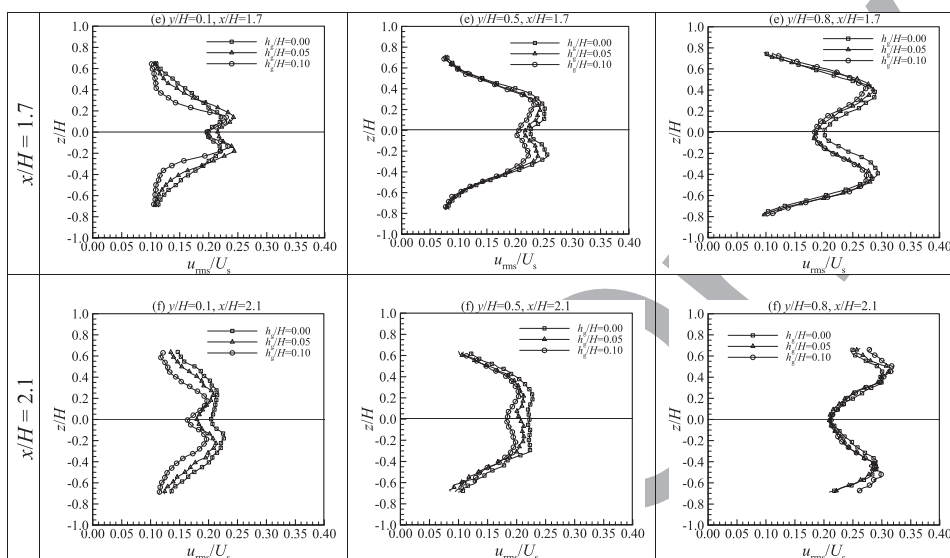
Figure 7. (*Continued*)

profiles at this streamwise location, and the largest magnitude of u_{rms}/U_s is reached by the
445   NGF case.

The u_{rms}/U_s profiles in the mid-depth and near-surface planes, shown in plots (b) to
(e) of Figure 7(ii) and 7(iii), illustrate that the off-axis peaks in the near-surface plane are
generally larger in magnitude ($u_{rms}/U_s \approx 0.40 \pm 0.02$) compared to the mid-depth plane
($u_{rms}/U_s \approx 0.32 \pm 0.02$). Moreover, the size of the valley also appears larger (smaller mag-
450   nitude of u_{rms}/U_s) in the near-surface plane compared to the mid-depth plane. However,
the magnitude of u_{rms}/U_s at $z/H = 0$ is approximately equal in the two planes ($\sim 0.14 \pm$
0.01). As the flow evolves in the downstream direction, plots (c) to (f) show a reduction in
the magnitude of the off-axis peaks from $x/H = 0.9$ to 2.1 for all gap height cases with a
corresponding increase in the valley region. Generally, the shape of the u_{rms}/U_s profiles in
455   the three planes seems to gradually approach a flat shape in the core region, which indicates
spreading out (redistribution) of the streamwise turbulence fluctuations u' in the horizontal
direction at downstream locations.

The development of the relative transverse turbulence intensity w_{rms}/U_s profiles in the
streamwise direction x/H is shown in Figure 8. Once again, the three columns in this figure
460   represent the profiles extracted from the horizontal planes at $y/H = 0.1$, 0.5, and 0.8. Plot
(a) of Figure 8(i)–(iii) demonstrates that the shape of the w_{rms}/U_s profiles at $x/H = 0.1$ is
also similar to the shape of the u_{rms}/U_s profiles. However, the peaks' magnitude of w_{rms}/U_s
is approximately one-half of u_{rms}/U_s values in the three planes. The w_{rms}/U_s profiles in the
near-bed plane, shown in plot (a) of Figure 8(i), display that the gap flow appears to cause
465   an increase in the peak values of w_{rms}/U_s in the SGF and LGF cases by $\sim 20\%$, while the
values in the valley/core region are increased by $\sim 29\%$, as compared with $w_{rms}/U_s \approx 0.15$
and 0.07, respectively, in the NGF case. However, the effect of the gap flow on the mid-
depth velocity field is mild, while its effect is negligible on the near-surface velocity field as
shown in plot (a) of Figure 8(ii) and 8(iii). As the flow develops to $x/H = 0.5$, plot (b) of

Figure 8(i)–(iii) displays that the transverse turbulence fluctuations w' increase and spread   470
in the three planes, but the rate is different. In the near-bed plane, it is shown that the off-axis
peaks of the w_{rms}/U_s profiles are about to disappear at this location. The profiles appear to
shrink slightly as the gap height increases, with a corresponding increase of w_{rms}/U_s in the
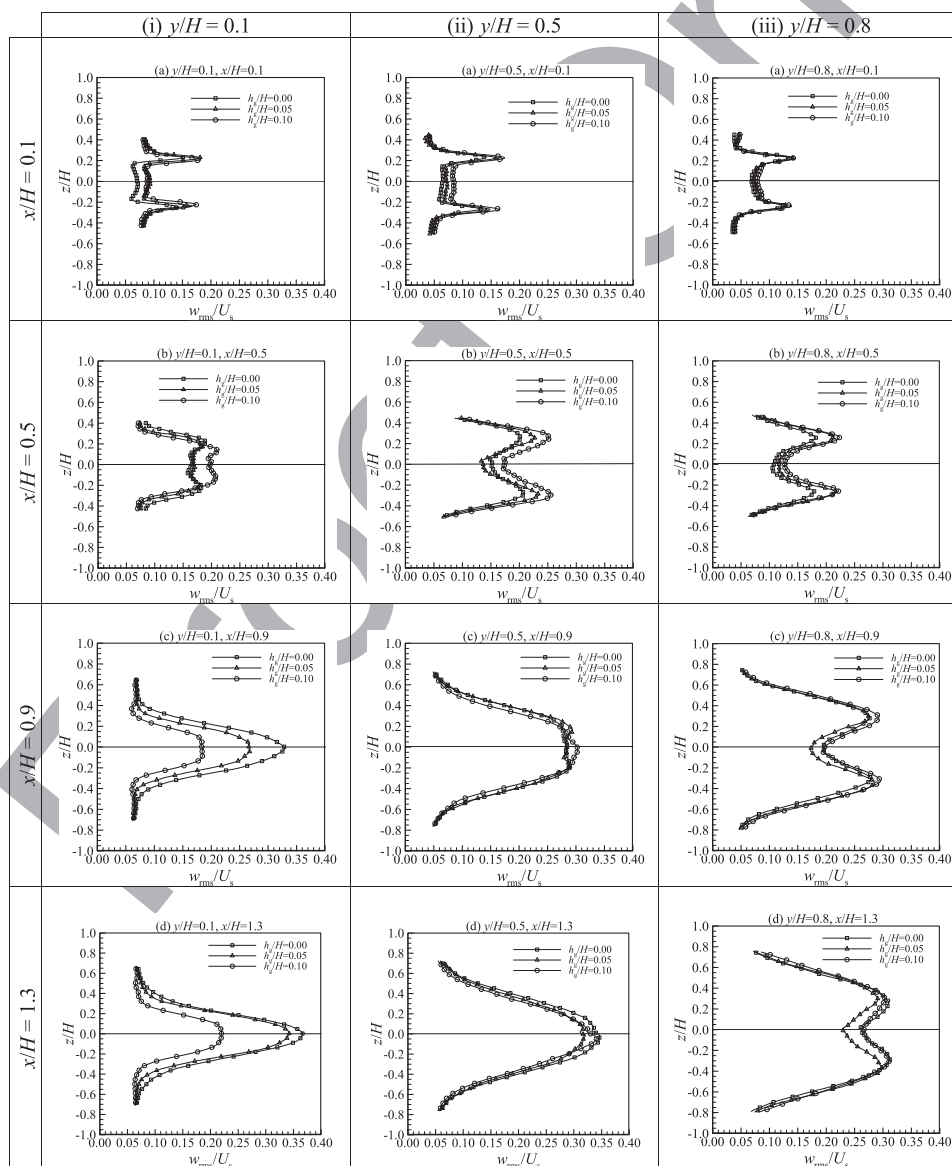core region ($|z/H| < 0.2$). However, the largest increase in the core region is attained by the

Figure 8. The relative transverse turbulence intensity w_{rms}/U_s profiles measured on the horizontal plane at; (i) $y/H = 0.1$, (ii) $y/H = 0.5$, and (iii) $y/H = 0.8$. Each column (i, ii, and iii) consists of six plots (a, b, c, d, e, and f) which display the development of w_{rms} profiles in the streamwise direction x. Each plot presents w_{rms}/U_s profiles for gap heights $h_g/H = 0.0$, 0.05, and 0.10. w_{rms} is normalised by U_s and z by the water depth H.
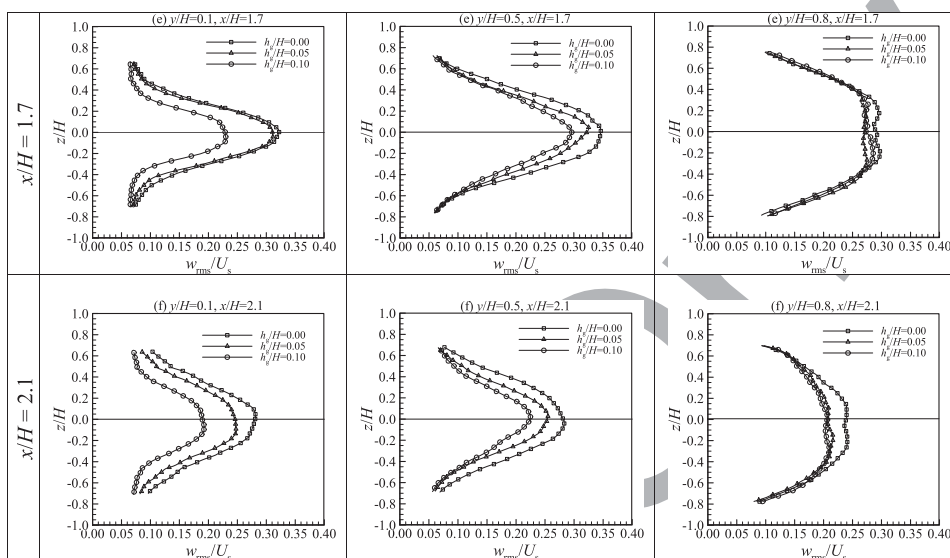
Figure 8. (*Continued*)

475   LGF case where the percentage of increase of w_{rms}/U_s is ~21% at $z/H = 0.0$. On the other side, the w_{rms}/U_s profiles in the mid-depth and near-surface planes at $x/H = 0.5$, shown in plot (b) of Figure 8(ii)–(iii), show that the profiles still consist of two off-axis peaks and a valley, and their outer region ($z/H > 0.3$) is relatively overlapped. However, there are some differences between the profiles in the two planes. For example, the profiles in the mid-
480   depth plane show that, although the transverse fluctuations w' in the LGF case increased by ~30% in the core region ($|z/H| < 0.3$), the SGF case demonstrates an increase of the peaks' fluctuations by ~15% and a reduction in the valley's fluctuations by ~12%, compared by the NGF case ($w_{rms}/U_s \approx 0.20$ and 0.15, respectively). Conversely, the transverse fluctuations w' of the SGF and LGF cases in the near-surface plane appear to increase in the core region
485   (~9% and ~18%, respectively), but their peaks' fluctuations are almost coincident, with an increase of ~22% compared to the NGF case.

As the flow develops in the streamwise direction, plots (c) to (e) in Figure 8 show a Gaussian/dome-type distribution of the w_{rms}/U_s profiles in the near-bed ($y/H = 0.1$) and mid-depth ($y/H = 0.5$) planes; while the profiles in the near-surface ($y/H = 0.8$) plane still
490   consists of two off-axis peaks and a valley which disappear at $x/H = 1.7$. In addition, the level of the transverse fluctuations w' is significantly increased in the three planes for $x/H \geq$ 0.9, compared to the corresponding results at the previous locations. However, the profiles in the near-bed plane, shown in plot (c) of Figure 8(i), demonstrate a significant reduction of the peak's fluctuations to ~19% and ~44% in the SGF and LGF cases, respectively, as a
495   result of the gap flow, compared to the NGF case ($w_{rms}/U_s \approx 0.33$). As well, the discrepancy between the SGF and NGF cases in the near-bed plane appear to decrease systematically in the downstream direction to become almost identical at $x/H = 1.7$ (see plots c to e). On the other hand, the profiles in the mid-depth plane, shown in plot (c) of Figure 8(ii), do not show such large discrepancy; they appear almost identical with a relatively small difference
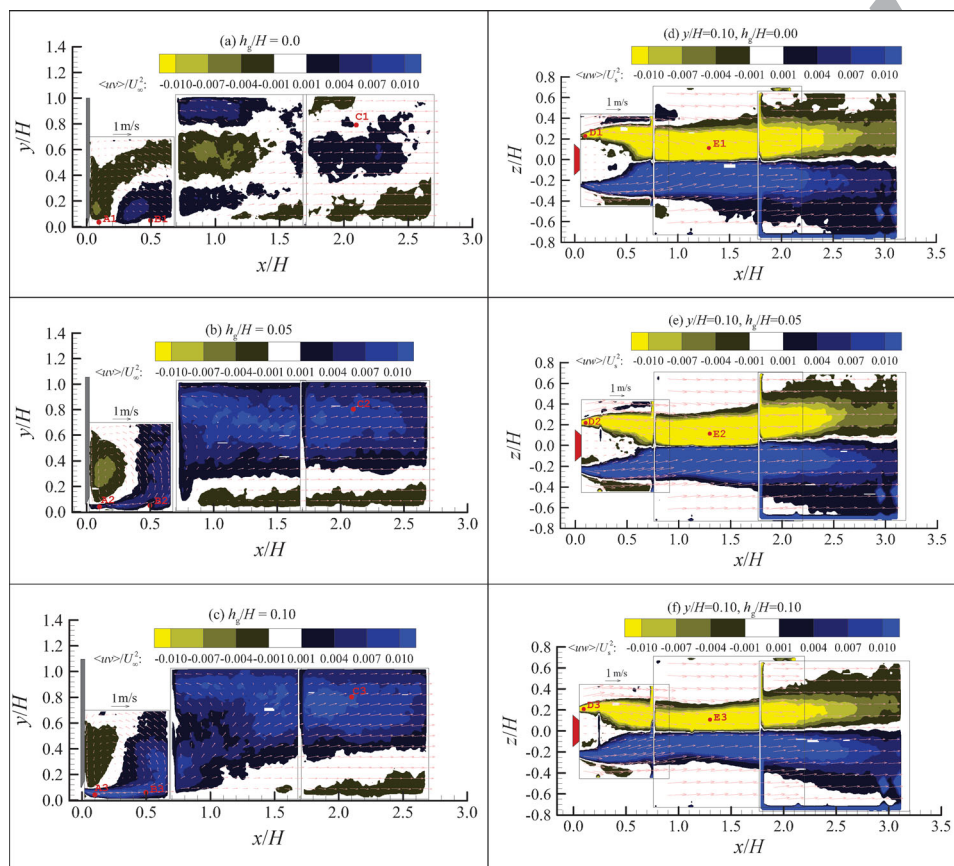500   ($w_{rms}/U_s \approx 0.29$). Similarly, the discrepancy between the profiles in the near-surface plane

Figure 9. Contours of the Reynolds shear stress $<uv>$ (a, b, and c) and $<uw>$ (d, e, and f) calculated on the vertical mid-plane ($z/H = 0$) and the horizontal near-bed plane ($y/H = 0.1$), respectively, superimposed on the mean velocity fields. Each row presents the results at a specific gap height ($h_g/H = 0$, 0.05, and 0.10). Locations (x, y, and z) are normalised by H, $<uv>$ by U_∞^2 and $<uw>$ by U_s^2.

is relatively small, where the magnitude of the off-axis peaks (for the three cases) is w_{rms}/U_s $\approx 0.28 \pm 0.01$, and of the valley ($z/H = 0$) is $w_{rms}/U_s \approx 0.19 \pm 0.01$. At further downstream, plots (e) to (f) of Figure 8(i)–(iii), illustrate the disappearance of the off-axis peaks and the valley shape in the three planes at $x/H = 1.7$ and 2.1. Moreover, the discrepancy between the three profiles in the three plots has increased, which is unexpected behaviour because the effect of the gap flow is expected to diminish at downstream locations and the velocity profiles collapse into a single profile at each vertical elevation. Generally, the behaviour at $x/H = 2.1$ is slight widening of the profiles with a corresponding decrease in the magnitude of the transverse turbulence fluctuations w'.

5.4. Reynolds stress

5.4.1. Reynolds stress contours
The distribution of the Reynolds shear stress on the vertical and horizontal planes is presented in Figure 9(a)–(f). Figure 9(a)–(c) displays the colour contour plots of $\langle uv \rangle/U_\infty^2$

on the vertical mid-plane ($z/H = 0$) velocity field at $h_g/H = 0$, 0.05, or 0.10, respec-
tively. It should be established that, near the bed, the ejection and sweep events are rep-
resented by negative $\langle uv \rangle$ (yellow colour), and outward and inward interactions by pos-
itive $\langle uv \rangle$ (blue colour), while near the free surface the events' signs are reversed. Figure
9(a) shows that the magnitude of $\langle uv \rangle/U_\infty^2$ appears small throughout the water layer
with some regions of relatively high positive magnitudes near the bed (first FOV) and
near the free surface (second FOV). For the SGF case ($h_g/H = 0.05$), there is a remark-
able change in the distribution of $\langle uv \rangle/U_\infty^2$ as shown in Figure 9(b). It can be seen that
positive $\langle uv \rangle$ becomes dominant from the free surface and down to about two-thirds of
the water depth, which appears to be correlated to the gap flow. However, the negative
$\langle uv \rangle$ can be seen in the near-bed region which suggests the frequent occurrence of ejec-
tion/sweep events. Similarly, the positive $\langle uv \rangle$ appears even more dominant in the LGF
case ($h_g/H = 0.10$) shown in Figure 9(c), as compared with the previous case, and cor-
related to the gap flow. However, the negative $\langle uv \rangle$ region near the bed appears to have
shrunk, which suggests suppression of the turbulence fluctuations as a result of the gap
flow.

The distribution of $\langle uw \rangle/U_s^2$ in the near-bed plane, shown in Figure 9(d)–(f), appears
to be symmetrical about the vertical mid-plane ($z/H = 0$) with larger magnitudes than
$\langle uv \rangle/U_\infty^2$. Moreover, these plots illustrate a slight reduction in the width of the colour con-
tours (narrowing) as the gap flow increases. More discussion about the Reynolds stress
results is given below.

5.4.2. Reynolds stress profiles

Vertical plane profiles. The Reynolds shear stress $\langle uv \rangle/U_\infty^2$ profiles measured on the ver-
tical mid-plane for the three gap heights $h_g/H = 0$, 0.05, and 0.10 are shown at different
streamwise locations in Figure 10(a)–(f). The first impression from these figures is the rel-
atively low Reynolds stress $\langle uv \rangle$ throughout the water depth at all streamwise locations,
which indicates a relatively low momentum exchange in this plane. Figure 10(a) illustrates
positive sharp spikes of $\langle uv \rangle$ at $x/H = 0.1$ near the bed for the SGF and LGF cases of mag-
nitudes 0.006 and 0.019 located at $y/H \approx 0.04$ and 0.06, respectively; while the magnitude
of $\langle uv \rangle$ for the NGF case is very small and negative. This indicates that the streamwise u'
and vertical v' fluctuations lie in the first and/or the third quadrant as will be discussed in
Section 7 . Away from the bed, the SGF and LGF cases becomes negative for $y/H > 0.07$
and 0.10, respectively, to approximately follow the NGF profile. The relatively low levels
of $\langle uv \rangle$ in all cases are not due to low u_{rms} and v_{rms} levels, but from a weak correlation of
the turbulent fluctuations u' and v'. Even near the bed, the magnitude of the peaks of u_{rms}
and v_{rms} for the gap-flow cases is not compatible with the peak values of $\langle uv \rangle/U_\infty^2$, which
confirms our conclusion.

The profiles at $x/H = 0.5$, shown in Figure 10(b), also illustrate that $\langle uv \rangle/U_\infty^2$ is still weak.
However, the sign of $\langle uv \rangle$ becomes positive in the SGF and LGF cases over the measured
water depth, while the NGF case appears positive in the range $y/H \leq 0.36$ and negative
for $y/H > 0.36$. The profile of the SGF case illustrates an increase in $\langle uv \rangle/U_\infty^2$ from zero on
the bed to approximately 0.005 at $y/H \approx 0.10$, and then becomes almost constant above this
point to the end of the curve. For the LGF case, it appears that $\langle uv \rangle/U_\infty^2$ increases to 0.011 at
$y/H \approx 0.07$, decreases slightly to 0.006 at $y/H \approx 0.15$, and then stays almost constant above
that. These results indicate that there is a slight enhancement in the momentum exchange
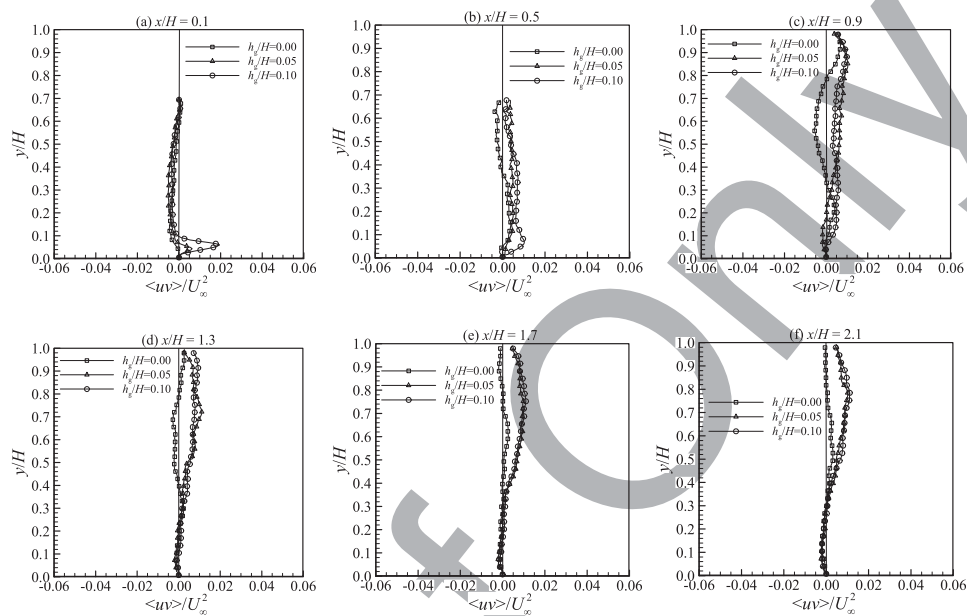
Figure 10. The relative Reynolds shear stress $<uv>/U_\infty^2$ profiles measured on the vertical mid-plane ($z/H = 0$) at different streamwise locations; (a) $x/H = 0.1$, (b) $x/H = 0.5$, (c) $x/H = 0.9$, (d) $x/H = 1.3$, (e) $x/H = 1.7$, and (f) $x/H = 2.1$. The Reynolds stress $<uv>$ is normalised by U_∞^2 and locations y by the water depth H.

in the vertical mid-plane because of the gap flow. However, the relatively large magnitudes of u_{rms} and v_{rms} are still not reflected in large $\langle uv \rangle$ because they seem to be uncorrelated.   560

As the flow moves downstream ($x/H = 0.9$ to 2.1), Figure 10(c)–(f) shows that the Reynolds shear stress $\langle uv \rangle$ for the NGF case appears to decrease gradually to become almost zero over the water depth. Conversely, the SGF and LGF cases demonstrate a small increase of $\langle uv \rangle$ in the upper region ($y/H > 0.36$) in the streamwise direction, while, in the lower region ($y/H \leq 0.36$), $\langle uv \rangle$ decreases to become almost zero at farther downstream locations   565 ($x/H = 0.5$ to 1.7). At $x/H = 2.1$, Figure 10(f) shows that $\langle uv \rangle$ is equal for the three cases in the lower region and seems to increase slightly in magnitude to become negative; while, in the upper region, $\langle uv \rangle$ of the SGF and LGF is almost identical with a maximum magnitude of $\langle uv \rangle/U_\infty^2 \approx 0.011$ at $x/H \approx 0.74$. From the above results, it can be concluded that the momentum exchange by the Reynolds stress is significantly weak in the vertical mid-plane   570 particularly in the lower half of the water depth.

Horizontal plane profiles. The Reynolds shear stress $\langle uw \rangle/U_s^2$ profiles extracted from the horizontal velocity fields at $y/H = 0.1$, 0.5, and 0.8 are shown in Figure 11(i)–(iii), respectively, at different streamwise locations. Plot (a) in Figure 11(i)–(iii) displays the $\langle uw \rangle/U_s^2$ profiles at $x/H = 0.1$ which appear to have two sharp spikes corresponding approximately   575 to the edges' position of the bluff body whereas $\langle uw \rangle \approx 0$ in the rest of the profiles. These plots show that the largest magnitude of $\langle uw \rangle/U_s^2$ occurs in the near-bed plane ($y/H = 0.1$), and their peaks' magnitude increases as the gap flow increases ($\langle uw \rangle/U_s^2 \approx 0.009$, 0.017, and 0.021 for $h_g/H = 0$, 0.05, and 0.10, respectively). Similarly, the $\langle uw \rangle/U_s^2$ profiles in the

580   mid-depth ($y/H = 0.5$) and near-surface ($y/H = 0.8$) planes, shown in plot (a) of Figure 11(ii)–(iii), illustrate that the effect of the gap flow on the velocity field is mild in the upper planes.

As the flow evolves downstream, plots (b)–(d) of Figure 11(i) illustrate a significant increase in the $\langle uw \rangle / U_s^2$ magnitude from $x/H = 0.5$ to 1.3 for all cases. However, the gap
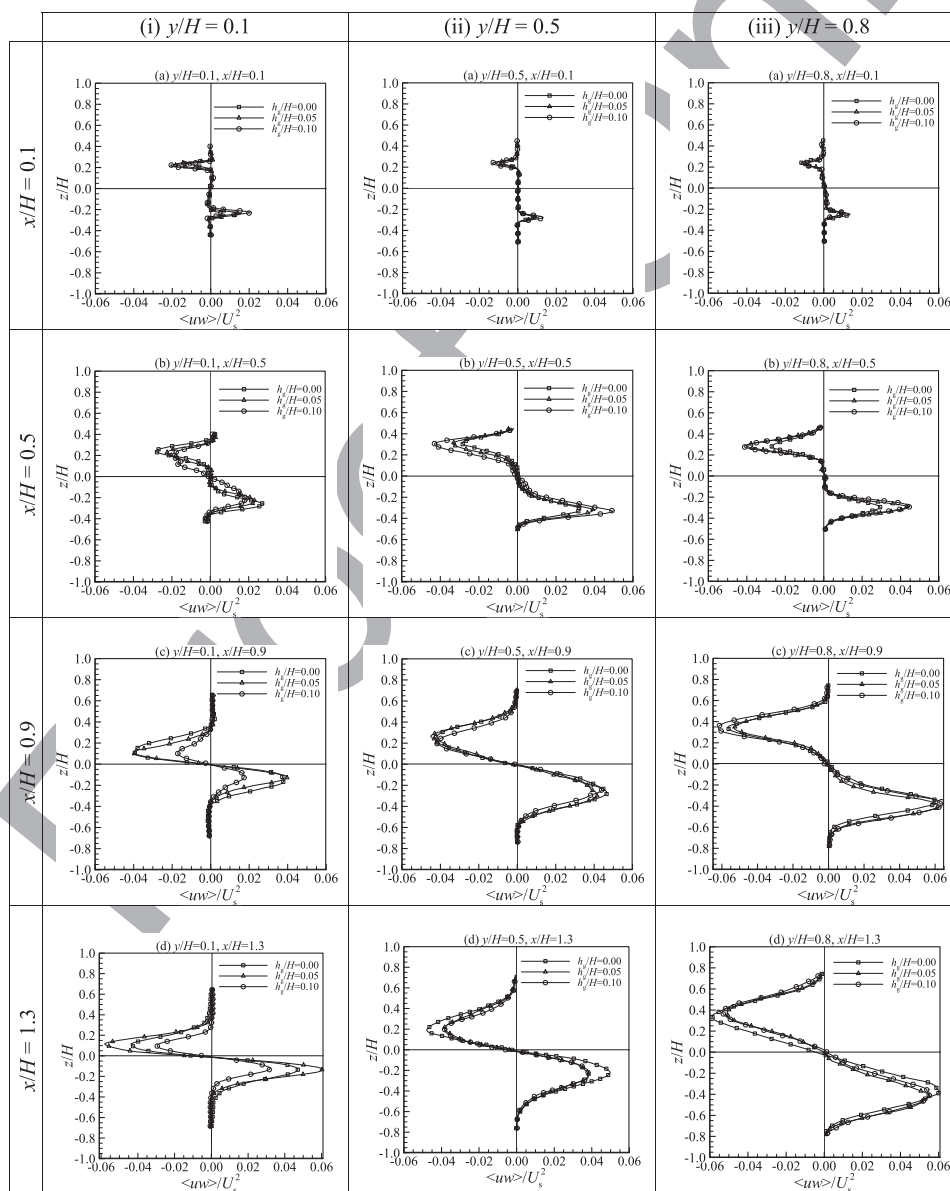

Figure 11. The relative Reynolds shear stress $\langle uw \rangle / U_s^2$ profiles measured on the horizontal plane; (i) $y/H = 0.1$, (ii) $y/H = 0.5$, and (iii) $y/H = 0.8$. Each column (i, ii, and iii) consists of six plots (a, b, c, d, e, and f) which display the development of $\langle uw \rangle / U_s^2$ profiles in the streamwise direction x. Each plot presents $\langle uw \rangle / U_s^2$ profiles for gap heights $h_g/H = 0$, 0.05, and 0.10. $\langle uw \rangle$ is normalised by U_s^2 and z by the water depth H.
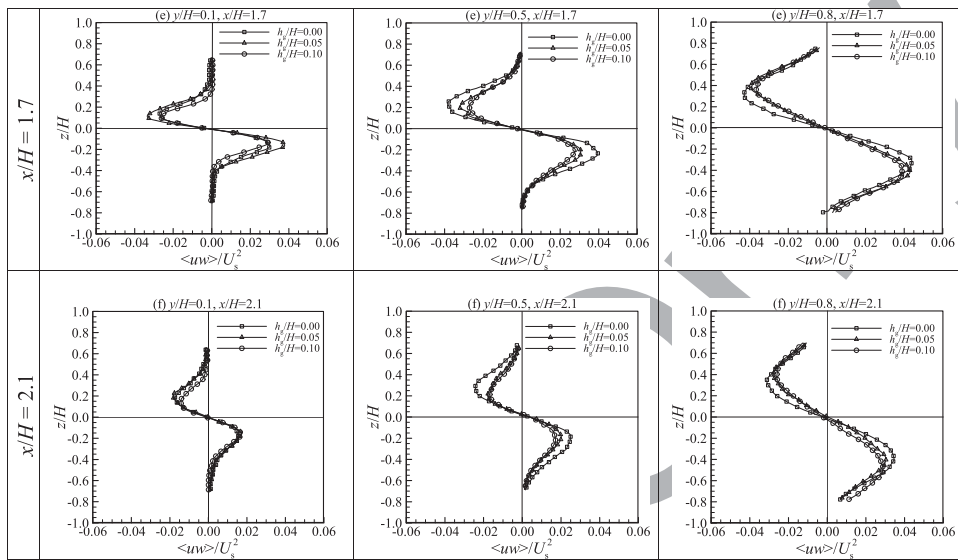
Figure 11. (*Continued*)

flow appears to attenuate the rate of increase of $\langle uw \rangle / U_s^2$ as demonstrated by the lower mag- 585
nitudes of $\langle uw \rangle / U_s^2$ in these plots with increasing the gap flow, compared to the NGF case.
At $x/H = 0.5$, the maximum magnitude of $\langle uw \rangle / U_s^2$ is 0.028, 0.023, and 0.018 for $h_g/H = $
0, 0.05, and 0.10, respectively, located at $|z/H| \approx 0.23 \pm 0.02$. The increase of the peaks'
magnitude continues in the streamwise direction to reach $|\langle uw \rangle / U_s^2| \approx 0.04$ at $x/H = 0.9$
for the NGF and SGF cases; while the LGF case remained unchanged as shown in plot (c) of 590
Figure 11(i). However, the location of the peaks appears to get closer to vertical mid-plane
($|z/H| \approx 0.11$). Similarly, the magnitude of $\langle uw \rangle / U_s^2$ continues to increase to $x/H = 1.3$,
where the largest magnitudes of $\langle uw \rangle$ are reached at this streamwise location in all cases.
The maximum absolute peak values are $|\langle uw \rangle / U_s^2| \approx 0.05$, 0.06, and 0.03 for $h_g/H = 0$,
0.05, and 0.10, respectively. It is interesting to see that the maximum magnitude is attained 595
in the SGF case ($h_g/H = 0.05$) in the near-bed plane. The high values of $\langle uw \rangle$ at this location
are consistent with the high levels of u_{rms} and w_{rms}, which indicate an increased correlation
of u' and w' and, consequently, enhancement of the momentum exchange by the Reynolds
stress. However, the LGF seems to be responsible for attenuating the correlation, while the
moderate gap flow enhanced it. 600

On the other hand, plots (b)–(d) in Figure 11(ii)–(iii) show that the profiles in the mid-
depth and near-surface planes appear wider than the profiles in the near-bed plane. In addi-
tion, the profiles appear to expand in the horizontal direction and increase in magnitude at
the downstream locations to reach the largest magnitude ($|\langle uw \rangle / U_s^2| \approx 0.040 \pm 0.05$ and
0.055 ± 0.05 for the mid-depth and near-surface planes, respectively) at $x/H = 1.3$. At far- 605
ther downstream locations, plots (e) and (f) in Figure 11(i)–(iii) illustrate that the $\langle uw \rangle / U_s^2$
profiles seem to have reached their maximum magnitudes at these locations, and started
declining in the downstream direction, which is consistent with the behaviour of u_{rms} and
w_{rms}. Moreover, the discrepancy between the profiles in the near-bed plane appears to van-
ish at this streamwise location. 610

In conclusion, the above results indicate that the Reynolds shear stress $\langle uw \rangle$ increases in the downstream direction in the three horizontal planes to reach their maximum magnitudes at $x/H = 1.3$. Afterwards, $\langle uw \rangle$ decreases in the streamwise direction. The gap flow is observed to increase $\langle uw \rangle$ in the near-bed plane when it is mild ($h_g/H = 0.05$), but its effect is mild in the mid-depth and near-surface planes. The $\langle uw \rangle$ profiles appear quite large/wide in the near-surface plane compared to the other planes particularly the near-bed plane. Generally, the Reynolds stress in the horizontal planes is strong indicating higher momentum exchange in the horizontal direction compared to the vertical mid-plane results.

6. Coherent structures

This section presents selected examples of large-vortical structures in the wake region educed by the proper orthogonal decomposition (POD) technique. The PIV velocity fields were first time-averaged and the fluctuations calculated. Then the POD method was applied to 2000 velocity fluctuation fields (of each case) using the method of snapshots.[27] A complete description of the implementation of the POD using the method of snapshots may be found in Shinneeb.[22] The number of modes used for the POD reconstruction in this paper was based on a target of ∼50% energy content and ranged from 6 to 28 modes. It should be noted that the vortical structures identified in the two-dimensional velocity fields represent only a cross-section of the vortical elements, and thus the discussions below reflect this fact. These POD-reconstructed velocity fields provide an interesting set of flow visualisation results. The purpose of this section is to provide instantaneous visualisation of vortical structures in the flow and, hence, to provide assistance to explain the behaviour of mean turbulence quantities and quadrant analysis results. It should be pointed out that the time separation between two consecutive velocity fields was 0.5 s which is too large to follow the same vortical structures in successive frames. However, some interesting features can be captured from individual fields. It should also be pointed out that this work produced a large amount of data, which cannot be presented here owing to space limitations. Consequently, only some selected examples are presented in this section, which highlight some interesting events that occur frequently (>90%) in the wake flow.

Figure 12 presents six selected examples of streamline plots to highlight the large-vortical structures of the wake flow. These examples are distributed into two columns and three rows; the first column (Figure 12(a)–(c)) represents the results on the vertical mid-plane ($z/H = 0$) for $h_g/H = 0$, 0.05, and 0.10, and the second column (Figure 12(d)–(f)) shows the results on the horizontal near-bed plane ($y/H = 0.1$). The locations (x, y, and z) are normalised by the water layer depth H. It should be pointed out that all vectors in all plots are scaled according to the reference vector to help the reader see the difference between the fluctuations' strength in different plots. At first glance, all plots shown in Figure 12 illustrate that the flow contains a large number of counter-rotating vortical structures that are distributed throughout the flow field at all times. In addition, Figure 12 also illustrates the interaction between the structures and the resulting induced flows. Figure 12(a) shows an interesting instantaneous outward radial flow (fluctuations) in all directions originating from a point that acts like a source (labelled A). Moreover, a clockwise (CW) rotating vortical structure (labelled B), whose axis is perpendicular to the x–y plane, appears to drive the flow to a point like a sink. These source- and sink-like structures illustrate an interesting behaviour of the instantaneous fluctuations which shed light on a possible mechanism
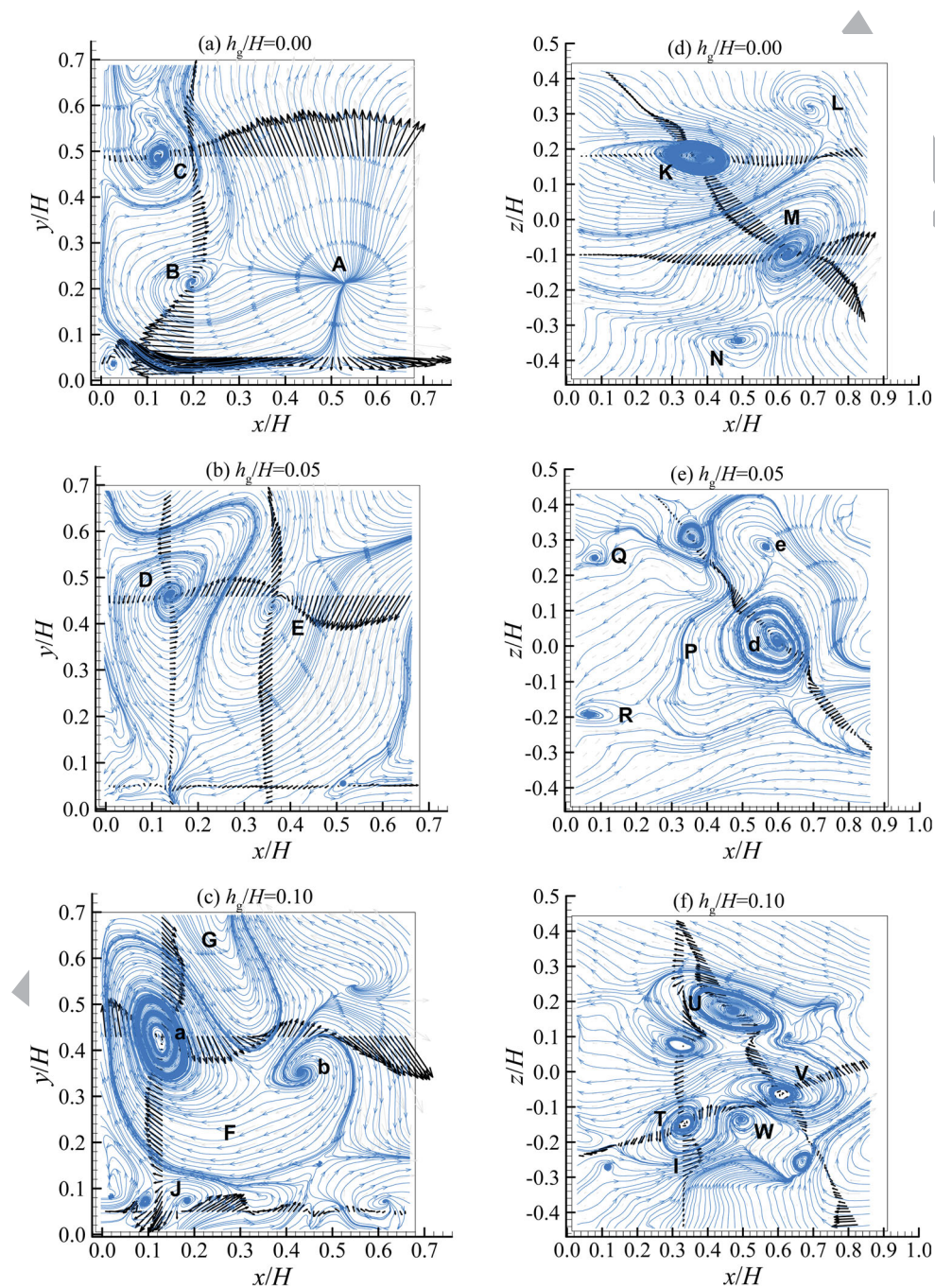
Figure 12. Streamline patterns of POD-reconstructed fluctuation velocity fields show vortical structures identified on the vertical mid-plane $z/H = 0.0$ (first column) and horizontal near-bed plane $y/H = 0.1$ (second column) for gap heights; (a, d) $h_g/H = 0$, (b, e) $h_g/H = 0.05$, and (c, f) $h_g/H = 0.10$. The turbulent kinetic energy recovered in these fields is ~50% using few modes. The induced flow by the structures is highlighted by superimposing velocity profiles at specific locations.

655   to transfer the flow (energy) from one plane (e.g. x–y plane) to another plane normal (or semi-normal) to the original plane. The outward radial flow induced by the source is very energetic in all directions (see the superimposed velocity profiles), and appears to change its direction as it approaches the solid wall. Another large structure that can be seen in this plot is the counter-clockwise (CCW) rotating structure (labelled C), which resides just

660   behind the bluff body in the mid-depth of the water layer. The induced flow by this structure is relatively weak compared to the source. It can be seen that the induced flow by the structures labelled A & B (near the bed) is very energetic and directed backward towards the bluff body, whereas the induced forward flow by the structures labelled B & C appears weaker because it is decelerated by the opposite flow of structure A. Figure 12(b) shows

665   another example of vortical structures (labelled D & E) on the vertical mid-plane for SGF case ($h_g/H = 0.05$). This figure reveals a pair of CW and CCW rotating vortices reside just behind the bluff body in the middle of the water layer. The proximity of the two structures from each other causes some distortion to their shapes, and the induced flow by the two strained structures D & E is directed upward, whereas the induced downward flow to the

670   right of structure E appears relatively energetic. Similarly, Figure 12(c) illustrates the presence of several structures for the LGF case ($h_g/H = 0.10$) whose axes are also perpendicular to the x–y plane. It is interesting to see a large distorted CW rotating structure (labelled F) with a large boundary and two cores (a and b) of same rotational sense, which appears to be in process to be torn apart. This conclusion is based on the fact that the vortical structures

675   that reside close to each other are usually counter-rotating (see [28]). It can be inferred that the penetration of structure G (only part of it is shown) into the side of structure F is responsible for splitting the structure core into two smaller cores a and b. Moreover, this plot also shows the presence of small structures that reside near the bed. Specifically, the small CCW structure labelled J appears to pump a strong jet upward at its right side and a downward

680   jet (towards the bed) at its left side, which suggests that this structure is a cross-section of a horseshoe element.[29]

   To shed light on the vortical structures in the horizontal plane, the selected examples are presented in Figure 12(d)–(f). Figure 12(d) shows cores of four structures of opposite rotational sense labelled K, L, M, and N, whose axes are perpendicular to the x–z plane.

685   The CW and CCW vortical structures labelled K and M are quite large and appear to pump a parcel of fluid backward towards the bluff body. In addition, the presence of unidirectional structures close to each other (labelled M and N) suggests that these structures were originally one large structure and was torn apart by the strained field generated by the interaction between the structures particularly by the CW flow near the right-bottom corner of

690   the FOV (seems to be a boundary of a large structure). Similar observation about the occurrence of the tearing process can also be seen in Figure 12(e), where a large CCW structure (labelled P) with a large boundary and two cores (labelled d and e). Moreover, this plot shows a pair of small CW and CCW structures (labelled Q and R) reside just behind the bluff body (at its edges), which seem to be newly formed. It is interesting to see that the level

695   of turbulence in this example is relatively low as reflected by the length of the vectors. Figure 12(f) shows another example of the vortical structures identified in the near-bed plane for the LGF case ($h_g/H = 0.10$). The presence of some unidirectional cores/structures in this plot (e.g. the cores labelled T, U, and V) close to each other also suggests that it was originally one big structure and torn apart into smaller structures. In addition, the penetration

700   of the CW structure (labelled W) between the two CCW structures labelled T and V seems

to be responsible for tearing them apart, and because of the induced jet labelled I, merging between the vortices W and V could occur. Unfortunately, these results do not tell us whether the increase in the tearing process is related to the gap flow or not; and due to space limitations, a separate investigation is required to characterise the effect of the gap flow on the large-vortical structures.

705

7. Quadrant analysis

Quadrant analysis is a commonly used statistical tool for investigating the Reynolds-stress-producing events in turbulent flows. The method decomposes the Reynolds shear stress into four distinct stress-producing events based on the quadrant in which they reside on the u'–v' (or u'–w') plane. In this study, the quadrant analysis was performed at selected points of high Reynolds shear stress regions. The purpose of this section is to quantify the energetic fluctuations at specific points and show the interactions between them. Since the ensemble size of the PIV data is 2000 velocity fields, three adjacent points were used at each location (from each velocity field) in the quadrant analysis in order to improve the conditional sampling of the extreme events. Thus, a total of 6000 data points were used to construct the plots shown below. The purpose of this section is to gain more insight into the effect of the gap flow on the turbulence events.

710

715

Figure 13(i)–(iii) shows the quadrant analysis performed at three selected points in the high mean Reynolds-stress regions identified on the vertical mid-plane ($z/H = 0$). This figure consists of nine plots distributed in three columns and three rows. Each column represents the results at a specific gap height ($h_g/H = 0$, 0.05, and 0.10); while the first two rows show the results of two points identified near the bed in the near-wake region, and the third row represents the results at a downstream location and near the free surface (see Figure 9). In these plots, the fluctuating velocity components u' and v' are normalised by the free stream velocity U_∞. The effect of the gap flow on u' and v' just behind the bluff body near the bed ($x/H = 0.1$ and $y/H = 0.03$) is presented in the first row (plot a) of Figure 13. Plot (a) of Figure 13(i) shows relatively small fluctuations u' and v' in the NGF case at this point (labelled A1 in Figure 9(a)), where most of them are clustered in a circle of approximately $0.2U_\infty$ radius with some scatter in the second quadrant. On the other hand, this distribution no longer exists in the gap-flow cases, i.e. there is a significant increase in the fluctuations in the SGF and LGF cases as shown in plot (a) of Figure 13(ii) and 13(iii), respectively. However, the predominant contribution of the Reynolds stress in the SGF case at this point (labelled A2 in Figure 9(b)) comes mainly from the positive events (the first quadrant, $+u'$ and $+v'$) which reaches ∼80% of U_∞; while the next contribution comes from the negative events (the fourth quadrant, $+u'$ and $-v'$). For the LGF case at the same point (labelled A3 in Figure 9(c)), the events mainly act in the negative u' direction (backward) where u'/U_∞ exceeded 80%; while most of the vertical fluctuations are negative (downwards) and their magnitude is $<0.4U_\infty$. It is interesting to see that similar to this event ($-u'$ and $-v'$) at the same point is induced by a vortical structure as visualised in Figure 12(c), which seems to occur frequently in this case. Since these events are generated by vortical structures, the discrepancy between different cases is likely due to the change in their distribution as a result of the gap flow.

720

725

730

735

740

At further downstream location ($x/H = 0.5$ and $y/H = 0.05$), the second row of Figure 13 illustrates a dramatic change in the distribution of the turbulence signals compared to the
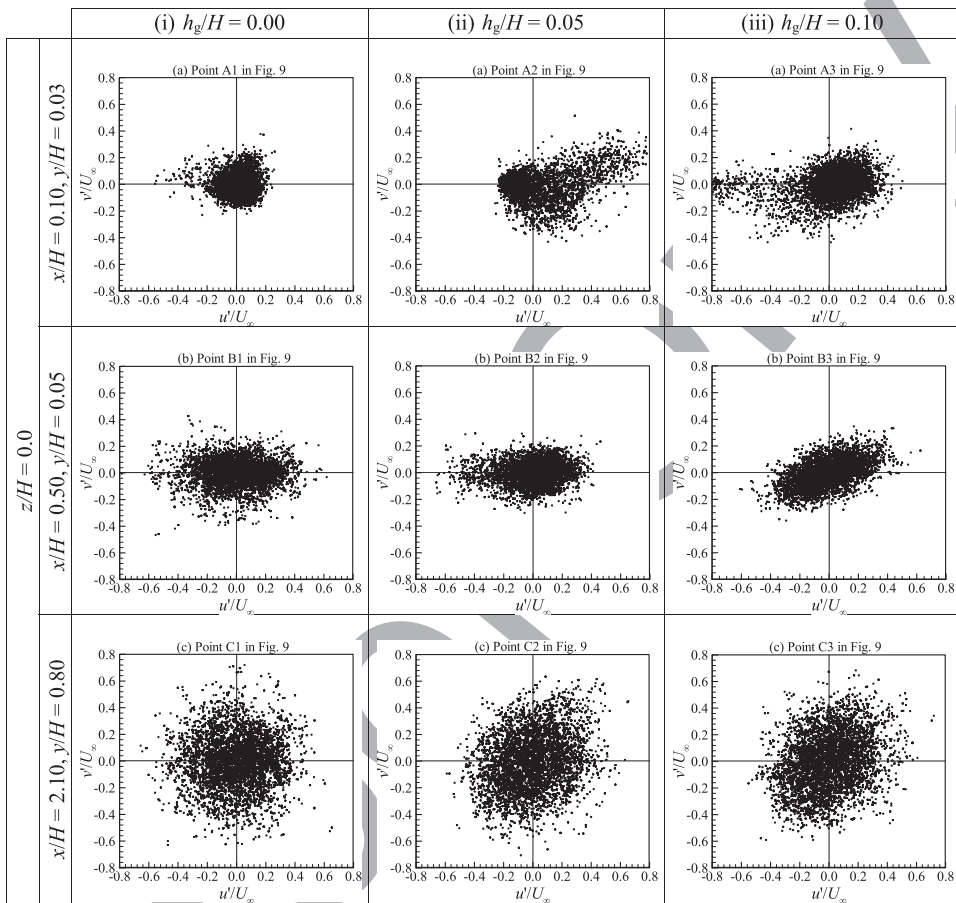
Figure 13. Quadrant analysis performed at selected points of the Reynolds shear stress fields on the vertical mid-plane ($z/H = 0$). Each column presents the results at a specific gap height ($h_g/H = 0$, 0.05, and 0.10) and each row presents the results at a specific position as labelled in Figure 9. Both u' and v' are normalised by U_∞.

745 previous location. Moreover, the effect of the gap flow appears to be mild on the SGF case, but it is significant on the LGF case. Specifically, the turbulence signals in the SGF case fluctuate at this point (labelled B2 in Figure 9(b)) along (and opposite to) the flow direction as in the NGF case [see plot (b) in Figure 13(i) and 13(ii)], although the bursting phenomenon is stronger in the opposite flow direction (negative u') in this case which approaches 60%
750 of U_∞. On the other hand, the distribution of the turbulence fluctuations in the LGF case at this point (labelled B3 in Figure 9(c)) appears elliptic, where its major axis (bursting direction) makes an angle of $\sim$30° with the horizontal, which means that the energetic fluctuating velocity signals act mainly in the first and third quadrants (negative production) with $|u'/U_\infty| \leq 0.4$ and $|v'/U_\infty| \leq 0.2$.
755   To assess the turbulence fluctuations near the free surface, the quadrant analysis was performed at farther downstream location ($x/H = 2.1$ and $y/H = 0.8$) at a point where the Reynolds stress is relatively high as shown in the third row (plot c) of Figure 13. From the first glimpse, the range of the turbulence signals appears larger compared to the previous
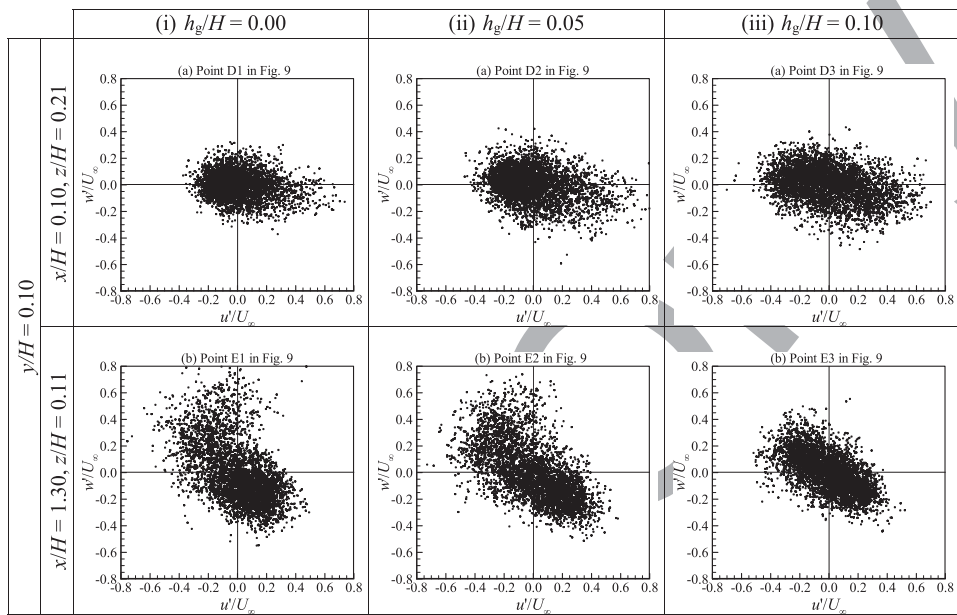
Figure 14. Quadrant analysis performed at selected points of the Reynolds shear stress fields on the near-bed plane ($y/H = 0.1$). Each column presents the results at a specific gap height ($h_g/H = 0$, 0.05, and 0.10) and each row presents the results at a specific position as labelled in Figure 9. Both u' and w' are normalised by U_∞.

results, particularly the vertical fluctuations v'. In the NGF case, the turbulence fluctuations at this point (labelled C1 in Figure 9(a)) are clustered in a circle of radius ∼$0.6U_\infty$ as shown   760 in plot (c) of Figure 13(i), which indicate an equal bursting in all directions. However, the SGF and LGF results, shown in plot (c) of Figure 13(ii) and 13(iii), which appear similar, illustrate that the fluctuating velocity at the same point (labelled C2 and C3 in Figure 9(b) and 9(c)) is clustered in a relatively elliptic shape, where its bursting direction makes an angle of ∼45° with the horizontal. According to the coordinate system, the line of action of   765 the turbulence fluctuations at this location is equivalent to the ejection and sweep events that occur near the bed, although it is relatively weak. In addition, these results explain the negligible magnitude of $<uv>/U_\infty$ in the NGF case because they cancel each other (see Figure 10(f)) and a relatively larger magnitudes of $<uv>/U_\infty$ in the SGF and LGF cases.

To shed light on the dynamics of the fluctuating velocity in the horizontal direction, the   770 quadrant analysis was performed at two points where the Reynolds shear stress $<uw>/U_\infty$ is relatively large. Since the near-bed plane is more affected by the gap flow, the two points were selected in this plane at two different streamwise locations ($x/H = 0.1$ and 1.3) as shown in Figure 14. To establish a good understanding of the behaviour of the fluctuations, it should be noted that w' is positive for outward fluctuations in the positive z/H side. The   775 first row of Figure 14 presents the results for three gap-height cases at $x/H = 0.1$ and $z/H = 0.21$, which correspond to the peak's location (see the points labelled D1, D2, and D3 in Figure 9). It is clear that most of the fluctuations in plot (a) of Figure 14(i) are clustered in a circle of radius $< 0.3U_\infty$ with some extreme events that lie in the fourth quadrant (positive u' and negative w'). This means that the energetic turbulence signals in the NGF case act in   780

the positive streamwise direction and towards the vertical mid-plane, where the direction of bursting makes approximately $-6°$ with the horizontal axis. Similarly, the fluctuations in the SGF and LGF cases also burst in the same direction as the NGF case, but with a relatively larger angle (approximately $-9°$ and $-10°$, respectively, from the horizontal axis). However, the strength of the velocity fluctuations appears to increase in magnitude as the gap flow increases, compared to the NGF case.

To assess the largest turbulence fluctuations in the near-bed plane that occur at $x/H = 1.3$, the analysis was performed at the peaks' position $z/H = 0.11$ (see the points labelled E1, E2, and E3 in Figure 9), and the results are shown in the second row of Figure 14. Plot (b) of Figure 14(i) illustrates the distribution of the turbulence signals for the NGF case which lie in the second and fourth quadrants. It is clear that the distribution is not symmetrical and is characterised by a large increase in the positive (outward) w' fluctuations to reach $\sim 0.8 U_\infty$ (negative w' is $< 0.5 U_\infty$), while the streamwise fluctuations u' is $< 0.6 U_\infty$. In addition, the contribution of the opposite sign fluctuating components is predominant at this location with a bursting direction of approximately $-34°$ measured from the horizontal axis. Similarly, the fluctuating velocities in the SGF case, shown in plot (b) of Figure 14(ii), burst in the same direction as in the previous case, but there is a slight decrease in the w' fluctuations as a result of the gap flow. However, these fluctuations produce the largest Reynolds stress $<uw>$ at this location as shown in plot (d) of Figure 11(i). On the other hand, plot (b) of Figure 14(iii), illustrate that the fluctuating velocities in the LGF are suppressed as a result of the gap flow, which is consistent with lowest value of $<uw>/U_\infty$ shown in Figure 11.

8. Conclusions

The following conclusions can be drawn from the results:

(1) The results revealed a gradual transfer of the TKE from the streamwise u_{rms} to the vertical v_{rms} component along the vertical mid-plane, and this transfer increases as the gap flow increases. In addition, there is a corresponding increase and spread of the transverse w_{rms} component in the transverse direction (in the three planes) as the flow evolves in the downstream direction, but with different rates. As well, the streamwise turbulence fluctuations u' generally spread out and become much larger at the sides of the wake region, but the gap flow causes narrowing of u_{rms} in the near-bed plane and widening in the near-surface plane. This narrowing is accompanied by an increase of the off-axis peaks in the small gap flow which suggests a redistribution of u_{rms} in the transverse direction; and by the energy transfer from the sides of the wake to the vertical mid-plane and then upward.

(2) The momentum exchange by the Reynolds stress is significantly weak in the vertical mid-plane particularly in the lower half of the water depth, which is not due to low u_{rms} and v_{rms} levels, but from a weak correlation of the turbulent fluctuations u' and v'. However, there is a slight enhancement in the momentum exchange because of the gap flow. On the other side, the Reynolds stress in the horizontal planes is strong indicating higher momentum exchange in the transverse direction compared to the vertical mid-plane results. This indicates an increased correlation of u' and w' in the transverse direction and, consequently, enhancement of the momentum exchange by the Reynolds stress. However, the LGF seems to be responsible for attenuating the correlation, while the moderate gap flow enhanced it.

(3) The flow contains a large number of counter-rotating vortical structures whose axes   825
are normal to the vertical (x–y) and horizontal (x–z) planes. The interaction between
the structures and the resulting induced flow seem to be responsible for deform-
ing and/or tearing apart the structures. The source and sink structures, that were
observed in the POD-reconstructed velocity fields, shed light on a possible mech-
anism to transfer the instantaneous flow/fluctuations (and hence the energy) from   830
one plane (e.g. x–y plane) to another plane normal (or semi-normal) to the original
plane.

(4) The events identified near the bed in the vertical mid-plane are affected significantly
by the gap flow if the point is very close to the jet, while the effect of the gap flow
at farther downstream locations becomes significant only if the gap flow is large.   835
Specifically, most of the energetic events in these cases come from the positive events
which lie in the first and/or third quadrants (inward and outward motion). As well,
the turbulence signals close the free surface, which lie in the first and third quad-
rants, appear larger than the near-bed events and is clustered in a relatively ellip-
tic shape, where its bursting direction makes an angle of ∼45º with the horizontal.   840
According to the adopted coordinate system, the line of action of the turbulence
fluctuations at this location is equivalent to the ejection and sweep events that occur
near the bed. All the fluctuations in these cases reach about 60% of the freestream
velocity. On the other hand, the major contribution to the Reynolds shear stress
in the horizontal near-bed plane comes from the opposite sign fluctuating com-   845
ponents which lie in the second and fourth quadrants (In the positive transverse
side, the line of action makes an angle with the positive streamwise direction mea-
sured CW towards the vertical mid-plane). The results revealed an increase in the
strength of the fluctuations near the edges of the bluff body as the gap flow increases.
Conversely, the fluctuating velocities at a farther downstream point (in the highest   850
Reynolds stress region) appear to be suppressed by the LGF, but the small gap flow
has negligible effect on them.

Acknowledgements

Disclosure statement

No potential conflict of interest was reported by the authors.

References

Q3

[1] Burger E, Wille R. Periodic flow phenomena. Ann Rev Fluid Mech. 1972;4:313–340.
[2] Wolanski E, Imberger J, Heron ML. Island wakes in shallow coastal water. J Geophys Res.
1984;89(6):10553–10569.
[3] Chen D, Jirka GH. Experimental study of plane turbulent wakes in a shallow water layer. Fluid   860
Dyn Res. 1995;16(1):11–41.
[4] Lloyd PM, Stansby PK. Shallow-water flow around model conical islands of small side slope –
Part I: surface piercing. J Hyd Eng. 1997;123:1057–67.

[5] Balachandar R, Tachie MF, Chu VH. Concentration measurement in intermediate shallow wakes. ASME J Fluids Eng. 1999;121(1):34–43.

[6] Nasif G, Barron RM, Balachandar R. DES evaluation of near-wake characteristics in a shallow flow. J Fluids Struct. 2014;45:153–163.

[7] Akilli H, Rockwell D. Vortex formation from a cylinder in shallow water: flow structure and topology. Phys Fluids. 2002;14(9):2957–2967.

[8] Singha A, Shinneeb A-M, Balachandar R. PIV-POD investigation of the wake of a sharp-edged flat bluff-body immersed in a shallow channel flow. ASME J Fluids Eng. 2009;131(2):021202–1 (12 pages).

[9] Bosch G, Kappler M, Rodi W. Experiments on the flow past a square cylinder placed near a wall. Exptl Thermal Fluid Sci. 1996;13:292–305.

[10] Bearman PW, Zdravkovich MM. Flow around a circular cylinder near a plane boundary. J Fluid Mech. 1978;89(1):33–47.

[11] Price SJ, Sumner D, Smith JG, et al. Flow visualization around a circular cylinder near to a plane wall. J Fluids Struct. 2002;16(2):175–191.

[12] Buresti G, Lanciotti A. Mean and fluctuating forces on a circular cylinder in cross-flow near a plane surface. J Wind Eng Industrial Aerodyn. 1992;41:639–650.

[13] Grass AJ, Raven PWJ, Stuart RJ, et al. The influence of boundary layer velocity gradients and bed proximity on vortex shedding from free spanning pipelines. ASME J Energy Resour Technol. 1984;106:70–78.

[14] Taniguchi S, Miyakoshi K. Fluctuating fluid forces acting on a circular cylinder and interference with a plane wall. Exp Fluids. 1990;9:197–204.

[15] Wang XK, Tan SK. Experimental investigation of the interaction between a plane wall jet and a parallel offset jet. Exp Fluids. 2007;42:551–562.

[16] Taniguchi S, Miyakoshi K, Dohda S. Interference between plane wall and two-dimensional rectangular cylinder. Trans Japan Soc Mech Eng Ser B. 1983;49(447):2522–2529.

[17] Durao DFG, Gouveia PST, Pereira JCF. Velocity characteristics of the flow around a square cross-section cylinder placed near a channel wall. Exp Fluids. 1991;11:298–304.

[18] Bailey SCC, Kopp GA, Martinuzzi RJ. Vortex shedding from a square cylinder near a wall. J Turbulence. 2002;3(3):1–18.

[19] Martinuzzi RJ, Bailey SCC, Kopp GA. Influence of a wall proximity on vortex shedding from a square cylinder. Exp Fluids. 2003;34:585–596.

[20] Krampa-Morlu FN, Balachandar R. A study on the flowpast a suspended bluff object in an open channel. Can J Civil Eng. 2001;28(4):547–554.

[21] Krampa-Morlu FN, Balachandar R. Flow recovery in the wake of a suspended flat plate. J Hyd Res. 2007;45(2):270–278.

[22] Shinneeb A-M. Confinement effects in shallow water jets [PhD thesis]. Canada: University of Saskatchewan; 2006.

[23] Shinneeb A-M, Bugg JD, Balachandar R. Variable threshold outlier identification in PIV data. Msmt Sci Tech. 2004;15:1722–1732.

[24] Huang H, Dabiri D, Gharib M. On errors of digital particle image velocimetry. Meas Sci Tech. 1997;8:1427–1440.

[25] Specialist Committee on Uncertainty Analysis of 25th ITTC. Uncertainty analysis – particle imaging velocimetry. International Towing Tank Conference; paper no. 7.5-01-03-03; 2008.

[26] Bugg JD, Rezkallah KS. An analysis of noise in PIV images. J Visualization. 1998;1(2):217–226.

[27] Sirovich L. Turbulence and the dynamics of coherent structures. Part I: coherent Structures. Q Appl Math. 1987;45(3):561–571.

[28] Shinneeb A-M, Bugg JD, Balachandar R. Coherent structures in shallow water jets. ASME J Fluids Eng. 2011;133(1):011203.

[29] Adrian RJ. Hairpin vortex organization in wall turbulence. Phys Fluids. 2007;19:233–270.

[30] Balachandar R, Bhuiyan F. Higher-order moments of velocity fluctuations in an open channel flow with large bottom roughness. J Hydraul Eng. 2007;133:77–87.

[31] Clauser F. Turbulent boundary layers in adverse pressure gradient. J Aerosp Sci. 1954;21:91–108.